A full orthotropic micropolar peridynamic formulation for linearly elastic solids

Vito Diana[a,*], Siro Casolo[a]

[a]*Department ABC, Politecnico di Milano, Italy*

Abstract

An original full orthotropic model for in-plane linear elasticity is proposed in the micropolar peridynamic analysis framework. The analytical formulation is derived from the definition of a specific microelastic energy function for micropolar nonlocal lattices which allows to obtain, for the first time, an orthotropic bond-based model characterized by four independent elastic moduli.

An important feature of the model is that the bond properties, i.e. the elastic constants, are continuous functions of the bond orientation in the principal material axes. The introduction of the bond shear stiffness and the definition of a bond shear deformation measure which accounts for particle's rotation, on one hand eliminates the restriction of two independent constants that affects other bond-based orthotropic peridynamic formulations, and on the other makes the model suitable in predicting the mechanical behavior of a wide variety of Cauchy orthotropic materials undergoing homogeneous and non-homogeneous deformations. The accuracy of the proposed model in linear elasticity has been verified through simulating uniaxial extension test of a composite lamina with a central circular hole and natural frequency analyses considering different orientations of the principal material reference system.

Keywords: Non-local lattice, Peridynamics, Orthotropy, Micropolar, Elasticity

1. Introduction

Peridynamics is a nonlocal theory of mechanics in which material points in a continuum or in a group of discrete particles interact with each other through forces that are functions of material and kinematic variables [1, 2]. Peridynamic (PD) theory replaces the differential equations of classical continuum mechanics with integro-differential equations without spatial derivatives and this aspect is particularly important for describing discontinuities in solid mechanics such as cracks. Much attention has been paid to isotropic materials, in order to solve the problem of the fixed Poisson's ratio. In fact, the PD model, as originally proposed (bond-based PD, i.e. BBPD) is a central force

*Corresponding author, e-mail: vito.diana@polimi.it

model, and therefore as in the rari-constant theory [3, 4], the Poisson's ratio is restricted to $\nu = 1/4$ for 3D and plane strain problems, and $\nu = 1/3$ for plane stress problems. To overcome this shortcoming, various efforts have been made. Silling et al. [5] introduced a more general formulation, coined state-based PD (SBPD) in which the pairwise forces between the particles are functions of the deformations of all nodes within the neighborhoods of the particles and the non-ordinary state-based model (NOSB), a tool for adapting classical material models for use with peridynamics and for simulating the material with advanced constitutive models [6]. In the context of bond-based models, instead, Liu and Hong [7] proposed an approach based on a force compensation scheme, Wang et al. [8, 9] derived a conjugated bond-pair-based peridynamic formulation in which the interacting forces between two material points within the horizon are not only related to the stretch of the bond, but also related to the rotation of the conjugated bond angles, and Zhu et al. [10] derived a PD formulation which accounts for single bond shear deformation to handle with different values of Poisson's ratio. Gerstle instead, introduced a two parameters micropolar isotropic PD model with Euler-Bernoulli beam-like microstructure [11]. PD theory has been used so far to model a wide variety of problems involving fracture [12, 13, 14, 15, 16], plasticity and viscoelasticy [17, 18, 19]. Anisotropic peridynamic models have been proposed by Colavito et al. [20], Xu et al. [21], Hu et al. [22], Hu and Madenci [23], and Oterkus and Madenci [24] to simulate crack propagation in unidirectional fibre-reinforced composites. These models are based on a homogenization approach in which the stiffness of the peridynamic bonds parallel to the fiber direction (fiber bonds) is fitted to the elastic modulus of the lamina in the same direction. All other bonds (matrix bonds) have their stiffness fitted to the lamina properties along the direction perpendicular to the fibers orientation. However, according to macro-mechanics of composite laminates, the stiffness (off-axis modulus) changes continuously with respect to the fiber orientation in a unidirectional lamina. Kilic and Madenci [25] developed a microscale PD model with fiber and matrix in separated material points, and predicted the matrix damage in laminated composites, accounting for the inhomogeneous distinct properties of the fiber and matrix. These models have been able to provide predictions of fiber/matrix fracture and delamination, which had good agreement with experimental observations. However, the model proposed in [25] requires a very detailed discretization of the spatial domain of interest, whereas the models presented in [21] and [24] require a uniform grid of particles and can be used to model plies with a certain mesh-friendly orientation of the fibers. The model presented by Hu et al. [26] for unidirectional fiber-reinforced composites can be used for any grid orientation relative to the fiber direction, however, like the other aforementioned orthotropic BBPD formulations, is characterized by fixed values of Poisson's ratio and shear modulus. In fact, they

stated to be effective to match modulus E_{11} and E_{22} and with the two remaining constants to be preset. Another anisotropic peridynamic model was described in Askari et al. [27], where the results of crack propagation in a poly-crystalline microstructure were also presented. Ghajari et al. [28] proposed for the first time a continuous model for orthotropic media with an eighth-order sinusoidal function and studied the failure modes of anisotropic materials. Similar PD formulations for orthotropic material were also proposed by Zhou et al. [29] and by Hu et al. [30]. However, since such orthotropic models are based on a classical bond-based PD formulation, only two independent material moduli can be chosen, whereas the other two result to be fixed. Recently, in the context of state-based peridymanics SBPD, an orthotropic PD model for linearly elastic solids was introduced by Mikata [31]. Another orthotropic SBPD model was proposed by Zhang and Quiao [32]. It can be seen that one limitation in SBPD or classical BBPD is that the bond force does not depends on the specific bond shear deformation but only on the bond extensional deformation [33, 34]. Moreover, state-based PD models come with a larger computational cost with respect to bond-based models [35].

In this paper, an original 2D generalized bond-based micropolar peridynamic formulation (MPPD) recently presented by the authors [36], is extended to orthotropic materials. Differently from other bond-based orthotropic peridynamic models with two independent material constants, the conceived model is based on the definition of a microelastic energy function which depends on three deformation parameters: the bond stretch, the bond shear deformation accounting for the rotational degrees of freedom, and the particles relative rotation. In this way, a bond-based peridynamic model for 2D Cauchy's orthotropic materials characterized by four independent material moduli, is obtained for the first time. Since three different stiffness parameters for each peridynamic ligament can be defined and calibrated separately, the model can be also useful to modelling Cosserat orthotropic materials. However in this paper we focus the attention on classical orthotropic materials. A distinctive aspect of this formulation is that all the bond stiffness constants are continuous functions of the bond orientation with respect to the principal material axes. The introduction of the bond shear stiffness and the definition of a bond shearing deformation measure which accounts for particles rotation enables the model to predict the mechanical behavior of a wide variety of Cauchy's orthotropic materials undergoing homogeneous and non-homogeneous deformations [36].

This paper is structured as follows. In Section 2, an analytical implicit linearized formulation of the proposed micropolar peridynamic model is given, handing particular attention to the numerical implementation aspects of the model. The novel generalized three parameter micropolar model is

derived starting from the definition of specific deformation measures related to shear and particles relative rotation deformations. In this way, the microelastic energy function is written, and the generalized bond stiffness operator for MPPD is obtained. The analytical expression of the four independent peridynamic constants for orthotropic materials are thus derived. The two parameter isotropic micropolar PD model is then obtained as a special case, by simply considering the shear and the axial stiffnesses as independent with the angle of inclination of the bond. In Section 3, we investigate the effectiveness of the MPPD formulation in elasticity and its capabilities in simulating the mechanical behavior of an orthotropic solid under homogeneous and non-homogeneous deformation fields, comparing the results with those obtained by FEM analyses. To this end, a natural frequency study and static analyses on a rectangular lamina with a central hole considering different orientations of the principal material reference system, are carried out. Finally, we resume the findings of this study and we discuss the results obtained. A MATLAB [37] computing on an UNIX OS is used to generate the results presented in this study.

2. Linearized Micropolar Peridynamics

In micropolar Peridynamics (MPPD) the particles translational degrees of freedom are augmented to include a rotational degree of freedom θ in two dimension [38]. In this way, the original equations of motion for any infinitesimal material particle at $\mathbf{X}$ in the reference configuration at time t are found from

$$\rho\ddot{\mathbf{u}}(\mathbf{X},t) - \int_{H_{\mathbf{X}}} \mathbf{f}(\mathbf{u}'-\mathbf{u},\mathbf{X}'-\mathbf{X})\mathrm{d}V_{\mathbf{X}'} - \mathbf{b}(\mathbf{X},t) = \mathbf{0} \quad \text{for} \quad \mathbf{X} \in \Omega, \tag{1}$$

$$\mathbf{J}\ddot{\boldsymbol{\theta}}(\mathbf{X},t) - \int_{H_{\mathbf{X}}} \mathbf{m}(\mathbf{u}'-\mathbf{u},\mathbf{X}'-\mathbf{X})\mathrm{d}V_{\mathbf{X}'} - \mathbf{c}(\mathbf{X},t) = \mathbf{0} \quad \text{for} \quad \mathbf{X} \in \Omega, \tag{2}$$

where Ω is the domain occupied by the body, whereas $\mathbf{X}'-\mathbf{X} = \boldsymbol{\xi}$ and $\mathbf{u}'-\mathbf{u} = \boldsymbol{\eta}$ are the relative position (i.e. reference bond) and the relative displacement between the material points $\mathbf{X}$ and $\mathbf{X}'$ (see Fig.1). The body force vector is $\mathbf{b}$, and $\mathbf{f}$ is the pairwise force in the peridynamic bond. The applied body couple is indicated by $\mathbf{c}$, and $\ddot{\boldsymbol{\theta}}$ is the angular acceleration vector, while $\mathbf{J}$ denotes the mass moment of inertia per unit volume tensor. The integrals are defined over a region $H_{\mathbf{X}}$ of radius δ (i.e. the horizon) [2]. The discretized form of the linear and angular momentuum equilibrium equations at time t are:

$$\sum_{j=1} \mathbf{f}(\mathbf{u}_j-\mathbf{u}_i,\mathbf{X}_j-\mathbf{X}_i)\Delta V_j + \mathbf{b}_i = \rho\ddot{\mathbf{u}}_{\mathbf{i}} \tag{3}$$

$$\sum_{j=1} \mathbf{m}(\mathbf{u}_j - \mathbf{u}_i, \mathbf{X}_j - \mathbf{X}_i)\Delta V_j + \mathbf{c}_i = \mathbf{J}\ddot{\boldsymbol{\theta}}_i \tag{4}$$

where subscript j denotes a particle within the horizon δ of particle i. Thus the sum in Eq. (3) is taken over all nodes j such that $|\mathbf{X}_j - \mathbf{X}_i| \leq \delta$ (i.e. neighboring particles of particle i). The computer code performs the discretization of the PD body using mesh generation tools developed for finite-element analyses. Then, the structure is discretized into a set of subvolumes, each of which has a single PD particle located at its centroid. Subsequently an algorithm determines the neighboring particles (i.e. the connections) of each particle of the discretization. A quadrature scheme in which partial neighbor intersections are also considered has been implemented. This aspect adds complexity to the creation of neighbor lists (Fig.2) but it increases the precision of the quadrature. The results of the partial neighbor intersection computation (i.e. the value of the volume correction coefficient α) is calculated by [7]

$$\alpha(|\boldsymbol{\xi}|) = \begin{cases} \frac{\xi - \delta + 0.5\Delta x}{\Delta x} & \text{if} \quad (\delta - 0.5\Delta x) < |\boldsymbol{\xi}| \leq \delta \\ 1 & \text{if} \quad |\boldsymbol{\xi}| \leq (\delta - 0.5\Delta x) \\ 0 & \textit{otherwise} \end{cases} \tag{5}$$

where Δx is the grid spacing. In the present implementation, the volume method for correcting the peridynamic surface effect is adopted [39, 40], thus the dimensionless correction factor for the micromoduli of the bond connecting two particles i and j is computed with

$$\lambda = \frac{2V_0}{V(H_i) + V(H_j)} \tag{6}$$

where V_0 is the ideal volume of $H_{\mathbf{X}}$, whereas $V(H_i)$ and $V(H_j)$ are the real volumes associated with H_i and H_j, respectively.

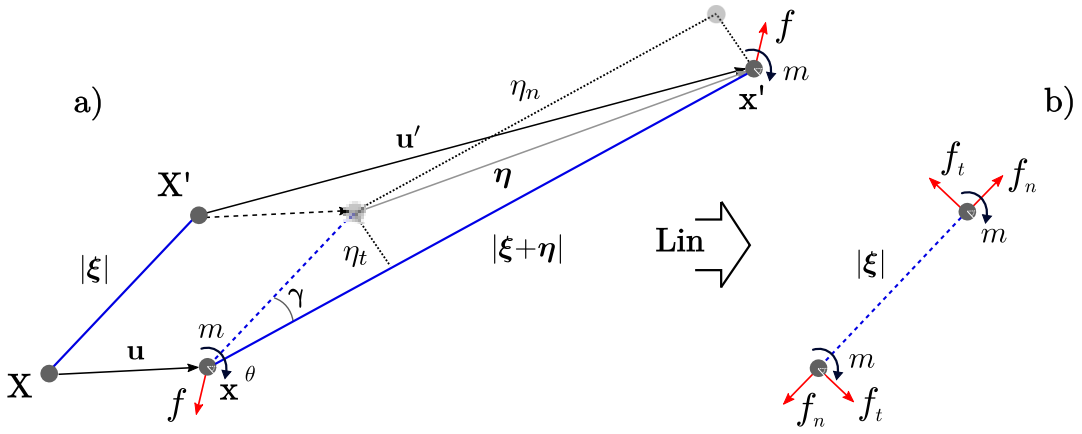

Figure 1: a) Undeformed and deformed configuration of a BBPD bond; b) Linearized BBPD (the pairwise force is directed along the line connecting the two particles in the undeformed configuration).

In micropolar peridynamics each bond connecting two particles i and j can be idealized as an assemblage of two translational spring and a rotational spring. The bond particle's force vector and the displacements in local coordinate system (e.g. quantities evaluated at the reference configuration aligned with the horizontal axis, as in Fig.3) are

$$\{f\}^T = \{f_n^i \quad f_t^i \quad m^i \quad f_n^j \quad f_t^j \quad m^j\} \tag{7}$$

and

$$\{u\}^T = \{u_n^i \quad u_t^i \quad \theta^i \quad u_n^j \quad u_t^j \quad \theta^j\} \tag{8}$$

This being a linearized micropolar peridynamic formulation, normal and tangential displacements are given with respect to coordinate axes that are aligned with the undeformed configuration. In this way we can define three bond deformation parameters, that are functions of the relative displacements in the normal, tangential, and rotational sense, respectively (see Fig. 3). The deformation in the normal direction is the bond stretch s,

$$s = \frac{|\boldsymbol{\xi} + \boldsymbol{\eta}| - |\boldsymbol{\xi}|}{|\boldsymbol{\xi}|} \tag{9}$$

which in a linearized theory is written as

$$s = \frac{1}{|\boldsymbol{\xi}|}\left(\boldsymbol{\eta} \cdot \frac{\boldsymbol{\xi}}{|\boldsymbol{\xi}|}\right) = \frac{\eta_n}{|\boldsymbol{\xi}|} = \frac{(u_n^j - u_n^i)}{|\boldsymbol{\xi}|} \tag{10}$$

where η_n is the component of $\boldsymbol{\eta}$ along the undeformed bond of unit vector $\boldsymbol{\xi}/|\boldsymbol{\xi}|$. The shearing deformation or bond sliding is

$$\gamma = \frac{(u_t^j - u_t^i)}{|\boldsymbol{\xi}|} - \frac{(\theta^j + \theta^i)}{2} \tag{11}$$

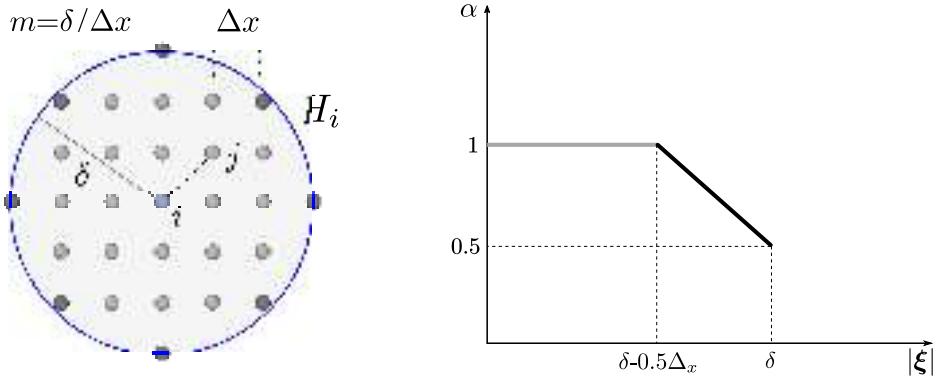

Figure 2: (sx) Proximity search procedure for neighboring list identification (in gray the full neighboring particles with $\alpha = 1$ and in black the partial neighboring particles);(dx) Volume correction coefficient α within the horizon. The ratio decreases to $1/2$ at the border of a horizon.

defined as the difference between the rotation angle of the beam chord and the particles average rotation. This latter reduces or increases the bond sliding depending on the mutual rotation sense of the particles itself. In particular, if the two particles rotate with an equal and opposite angle θ, the rotation contribute to the bond sliding is null. We can also introduce a deformation parameter

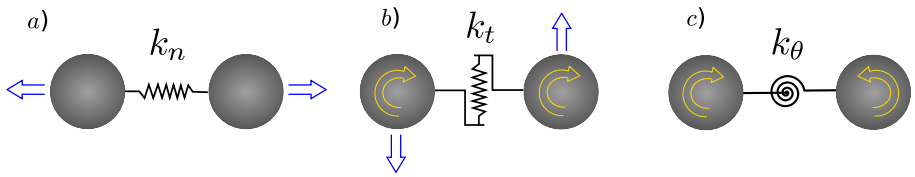

Figure 3: Sketch of the interactions between two particles: a) due to normal spring, b) due to shearing spring, c) due to rotational spring.

for the rotational bond spring which is defined by the relative particles rotation measure, or in other words the difference between the rotation angles of the two connected particles

$$\vartheta = (\theta^j - \theta^i) \tag{12}$$

This parameter can be used to improve the bond stretch measure in such a way that

$$s = \frac{(u_n^j - u_n^i) + \kappa\vartheta}{|\boldsymbol{\xi}|} \tag{13}$$

where κ is a scaling parameter which regulates how much bending is considered in the bond stretch measure (usually, for simplicity is set to zero)[41, 42, 43]. In this way we can write the kinematic relations between the particles displacements and the bond deformation parameters

$$\{h\} = [B]^T\{u\} \tag{14}$$

where $\{h\} = \{s \quad \gamma \quad \vartheta\}^T$ is the vector of the springs deformation measures and $[B]^T$ is defined as

$$[B]^T = \frac{1}{|\boldsymbol{\xi}|}\begin{bmatrix} -1 & 0 & 0 & 1 & 0 & 0 \\ 0 & -1 & |\boldsymbol{\xi}|/2 & 0 & 1 & |\boldsymbol{\xi}|/2 \\ 0 & 0 & -|\boldsymbol{\xi}| & 0 & 0 & |\boldsymbol{\xi}| \end{bmatrix} \tag{15}$$

The constitutive behavior of the model is defined by the following relation

$$\{q\} = [D]\{h\} \longrightarrow \begin{Bmatrix} f_n \\ f_t \\ m_\theta \end{Bmatrix} = \begin{bmatrix} k_n & 0 & 0 \\ 0 & k_t & 0 \\ 0 & 0 & k_\theta \end{bmatrix} \begin{Bmatrix} s \\ \gamma \\ \vartheta \end{Bmatrix} \tag{16}$$

where $[D]$ is a diagonal matrix [1] containing the bond normal, tangential, and rotational spring equivalent stiffnesses, and relates the pairwise forces and microcouple, (i.e. the peridynamic actions between two particles) to the parameters of bond deformation defined above. The pairwise bond couple and forces can be viewed as the springs reactions to the bond deformations s and γ and r, respectively. In particular, the bond forces are equal in modulus to the particles forces ($f_n = f_n^j = -f_n^i$ and $f_t = f_t^j = -f_t^i$) but this is not true for bond and particles couples. In fact, for example, happens that m_i and m_j could assume the same nonzero value leading to a bond microcouple m_θ equal to zero. This because, m_θ represents the self-equilibrated part of the particles microcouples in a specific ligament.

It is worth noting that this is a general micropolar Peridynamic formulation which leads to different centrosymmetric models depending on the specific constitutive parameters laws k_n, k_t and k_θ adopted.

The general form of the microelastic energy density $\Phi(\mathbf{X})$ for micropolar peridynamics is obtained by considering the contribution of the three springs and their corresponding deformation measures

$$\Phi(\mathbf{X}) = \frac{1}{2}\int\limits_{H_\mathbf{X}} \frac{k_n s^2|\boldsymbol{\xi}|}{2} + \frac{k_t \gamma^2|\boldsymbol{\xi}|}{2} + \frac{k_\theta \vartheta^2}{2} \mathrm{d}V_{\mathbf{X}'} \tag{17}$$

In this way, considering the definition of the macroelastic potential energy for a micropolar peridynamic body

$$\hat{\Phi}(\mathbf{X}) = \frac{1}{2}\int\limits_{\Omega}\int\limits_{H_\mathbf{X}} \frac{k_n s^2|\boldsymbol{\xi}|}{2} + \frac{k_t \gamma^2|\boldsymbol{\xi}|}{2} + \frac{k_\theta \vartheta^2}{2} \mathrm{d}V_{\mathbf{X}'} dV_\mathbf{X} \tag{18}$$

for a single bond of length $|\boldsymbol{\xi}|$ between two particles i and j (see Fig.4), we can write a discrete form of the balance of the variation of the total macroelastic energy and the work W done by the external nodal forces $\{p\}$ (in the hypothesis of small deformations, i.e. linearized PD) as

$$\hat{\Phi} = \frac{1}{2}\{u\}^T \frac{1}{2}[B][D]\Delta V_i |\boldsymbol{\xi}| \alpha \Delta V_j [B]^T \{u\} = \frac{1}{2}\{u\}^T \{p\} = W \tag{19}$$

[1] When considering orthotropic materials, the $[D]$ matrix which describes the constitutive behavior of the bond is dependent on the orientation (ψ) angle of the ligament.

In this way the bond stiffness matrix in global coordinate system can be expressed in the following form

$$[K]_{bond} = \alpha|\boldsymbol{\xi}|\Delta V_i \Delta V_j [R]^T [B][D][B]^T [R] =$$

$$= \frac{\alpha}{|\boldsymbol{\xi}|}\Delta V_i \Delta V_j [R]^T \begin{bmatrix} k_n & 0 & 0 & -k_n & 0 & 0 \\ 0 & k_t & -k_t|\boldsymbol{\xi}|/2 & 0 & -k_t & -k_t|\boldsymbol{\xi}|/2 \\ 0 & -k_t|\boldsymbol{\xi}|/2 & k_\theta|\boldsymbol{\xi}| + k_t|\boldsymbol{\xi}|^2/4 & 0 & k_t|\boldsymbol{\xi}|/2 & -k_\theta|\boldsymbol{\xi}| + k_t|\boldsymbol{\xi}|^2/4 \\ -k_n & 0 & 0 & k_n & 0 & 0 \\ 0 & -k_t & k_t|\boldsymbol{\xi}|/2 & 0 & k_t & k_t|\boldsymbol{\xi}|/2 \\ 0 & -k_t|\boldsymbol{\xi}|/2 & -k_\theta|\boldsymbol{\xi}| + k_t|\boldsymbol{\xi}|^2/4 & 0 & k_t|\boldsymbol{\xi}|/2 & k_\theta|\boldsymbol{\xi}| + k_t|\boldsymbol{\xi}|^2/4 \end{bmatrix} [R] \quad (20)$$

where $[R]$ is a rotation matrix. It can be noted that in Eq.17, the factor 1/2 is included because the energy stored in each bond is associated equally with the two particles connected by the ligament. In this way, following Eqs. 18 and 19 one can derive the expression of the half-bond stiffness matrix. For this reason, being Eq.20 referred to the entire bond, the factor 1/2 is removed from that equation. In any case on has to consider this aspect in order to avoid double-counting of the bonds $i - j$ and $j - i$. After the assembly of the global structure stiffness matrix, the displacements and forces can be determined in the usual manner.

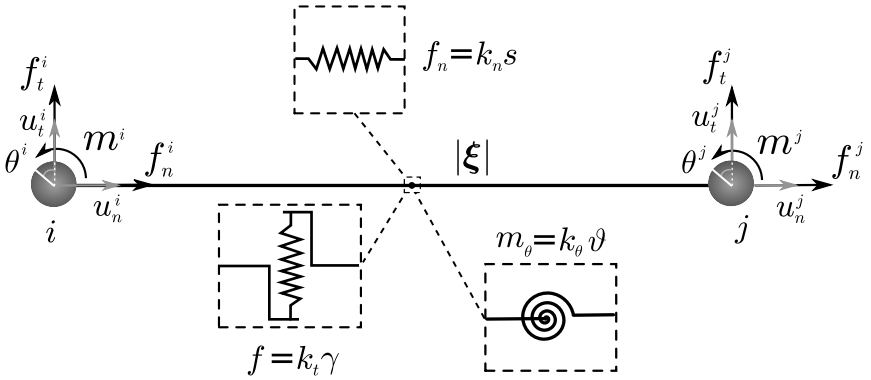

Figure 4: Schematics of bond configuration connecting two particles i and j in the local coordinate system for bond-based micropolar peridynamics. The bond can be idealized as a set of three (axial, shear and rotational) equivalent springs placed in midpoint of the ligament.

Since the introduction of rotational degrees of freedom into the lattice spring models provides the stiffness matrix resembling the beam stiffness matrix, beams come as a natural choice to represent (non-local) lattice elements[44]. The micro-elastic energy of a micropolar peridynamic solid with frame-like ligaments connecting particles, thus a 2D non-local lattice with Euler-Bernoulli beam-like microstructure (i.e. Gerstle's micropolar model [11]), is a special case of the model described here by Eqs.(17) and (20).

It is worth noting that in bond-based micropolar isotropic Gerstle's model, any bond shear deformation parameter is directly defined and the microelastic energy density $\Phi(\mathbf{X})$ can be written in the form

$$\Phi(\mathbf{X}) = \frac{1}{2}\int_{H_{\mathbf{X}}} \frac{k_n s^2|\boldsymbol{\xi}|}{2} + \frac{k_\chi \chi^2|\boldsymbol{\xi}|}{2} \mathrm{d}V_{\mathbf{X}'} \tag{21}$$

where $k_n = c$ and $k_\chi = d$, are the axial and bending micromodulus functions defined in [11], whereas χ is a bond deformation parameter associated to the bond curvature. However, by using the bond deformation parameters introduced by the authors and defined in Eqs. (11)-(12) and the constitutive law of Eq. (16), Gerstle's model can be derived assuming

$$\begin{aligned} k_n &= c \\ k_t &= 12d/|\boldsymbol{\xi}|^2 \\ k_\theta &= d/|\boldsymbol{\xi}| \end{aligned} \tag{22}$$

where, differently from the conceived model [36], the independent elastic constants are only two, since $k_t = f(k_\theta)$. In other words the rotational stiffness k_θ of the bond is directly determined by the shearing stiffness k_t of the ligament, and thus its value cannot be changed.

In this specific case Eq.(20) becomes

$$[K]_{bond} = \frac{\alpha}{|\boldsymbol{\xi}|}\Delta V_i \Delta V_j [R]^T \begin{bmatrix} c & 0 & 0 & -c & 0 & 0 \\ 0 & 12d/|\boldsymbol{\xi}|^2 & -6d/|\boldsymbol{\xi}| & 0 & -12d/|\boldsymbol{\xi}|^2 & -6d/|\boldsymbol{\xi}| \\ 0 & -6d/|\boldsymbol{\xi}| & 4d & 0 & 6d/|\boldsymbol{\xi}| & 2d \\ -c & 0 & 0 & c & 0 & 0 \\ 0 & -12d/|\boldsymbol{\xi}|^2 & 6d/|\boldsymbol{\xi}| & 0 & 12d/|\boldsymbol{\xi}|^2 & 6d/|\boldsymbol{\xi}| \\ 0 & -6d/|\boldsymbol{\xi}| & -2d & 0 & 6d/|\boldsymbol{\xi}| & 4d \end{bmatrix} [R] \tag{23}$$

thus the same expression of the bond stiffness matrix described in [45] is obtained.

2.1. A full orthotropic peridynamic model

In the classical theory of elasticity, the stress-strain relations (Hooke's law) for an orthotropic material under plane-stress or plane-strain conditions in the principal material system, inclined at angle ζ with respect to the horizontal, can be written using the Voigt notation as:

$$\{\sigma\} = [\mathbf{C}]\{\epsilon\} \longrightarrow \begin{Bmatrix} \sigma_1 \\ \sigma_2 \\ \tau_{12} \end{Bmatrix} = \begin{bmatrix} C_{11} & C_{12} & 0 \\ C_{12} & C_{22} & 0 \\ 0 & 0 & C_{66} \end{bmatrix} \begin{Bmatrix} \epsilon_1 \\ \epsilon_2 \\ \gamma_{12}^* \end{Bmatrix} \tag{24}$$

where

$$C_{11} = \frac{E_{11}}{1-\nu_{12}\nu_{21}}; \qquad C_{22} = \frac{E_{22}}{1-\nu_{12}\nu_{21}}; \qquad C_{12} = \frac{\nu_{21}E_{11}}{1-\nu_{12}\nu_{21}}; \qquad C_{66} = G \tag{25}$$

with $\nu_{12} = \nu_{21}E_{11}/E_{22}$. Assuming here for simplicity that $\zeta = 0$ and thus considering a generic coordinate system xy rotated by ψ with respect to the horizontal, Eq.(24) can be rewritten as

$$\{\sigma\}^{\psi} = [\mathbf{C}]^{\psi}\{\epsilon\}^{\psi} \tag{26}$$

being $[\mathbf{C}]^{\psi}$ defined as

$$[\mathbf{C}]^{\psi} = \begin{bmatrix} C_{xx} & C_{xy} & C_{xs} \\ C_{xy} & C_{yy} & C_{ys} \\ C_{xs} & C_{ys} & C_{ss} \end{bmatrix} = [\mathbf{Q}]^{-1}[\mathbf{C}][\mathbf{Q}]^{-T} = [\mathbf{Q}]^{-1} \begin{bmatrix} C_{11} & C_{12} & 0 \\ C_{12} & C_{22} & 0 \\ 0 & 0 & C_{66} \end{bmatrix} [\mathbf{Q}]^{-T} \tag{27}$$

where $[\mathbf{Q}]$ is

$$[\mathbf{Q}] = \begin{bmatrix} \cos^2\psi & \sin^2\psi & 2\cos\psi\sin\psi \\ \sin^2\psi & \cos^2\psi & -2\cos\psi\sin\psi \\ -\cos\psi\sin\psi & \cos\psi\sin\psi & \cos 2\psi \end{bmatrix} \tag{28}$$

Thus, the off-axis axial C_{xx} and shear C_{ss} moduli can be written as function of the direction defined by ψ, in terms of the four material constants defined in Eq. (25) as

$$C_{xx}(\psi) = C_{11}\cos^4\psi + C_{22}\sin^4\psi + 2C_{12}\sin^2\psi\cos^2\psi + 4C_{66}\sin^2\psi\cos^2\psi \tag{29}$$

$$C_{ss}(\psi) = C_{11}\sin^2\psi\cos^2\psi + C_{22}\sin^2\psi\cos^2\psi - 2C_{12}\sin^2\psi\cos^2\psi + C_{66}(\cos^2\psi - \sin^2\psi)^2 \tag{30}$$

By analogy with the continuum, we can assume for instance that in an orthotropic peridynamic solid, k_n and k_t follow a law of variation with respect to ψ similar to that of C_{xx} and C_{ss} described by Eqs. (29) and (30), respectively, in such a way that

$$k_n(\psi) = k_{n_1}\cos^4\psi + k_{n_2}\sin^4\psi + 2k_\nu\sin^2\psi\cos^2\psi + 4k_{t_1}\sin^2\psi\cos^2\psi \tag{31}$$

$$k_t(\psi) = k_{n_1}\sin^2\psi\cos^2\psi + k_{n_2}\sin^2\psi\cos^2\psi - 2k_\nu\sin^2\psi\cos^2\psi + k_{t_1}(\cos^2\psi - \sin^2\psi)^2 \tag{32}$$

where k_{n_1} and k_{n_2} are the peridynamic axial micromoduli along principal material axes, k_{t_1} is the shear micromodulus along one of the principal material axis [2] and k_ν is a parameter which regulates the ratio between $k_t(\psi)$ and $k_n(\psi)$ in each direction. Thus we have defined four peridynamic micromoduli for describing the mechanical behavior of a 2D orthotropic solid. In order to obtain the relation between the orthotropic peridynamic bond stiffness constants, k_{n_1}, k_{n_2}, k_ν and k_{t_1} and

[2] In Cauchy orthotropic materials in fact, $G_{11} = G_{22} = G$, hence $k_{t_1} = k_{t_2}$ [46].

the classical continuum elastic moduli defined in Eq. (25), the approach introduced by Gerstle et al.[45] is used. Given a specific strain state, the strain energy density in a specific point was determined from the peridynamic formulation and it was set equal to the strain energy determined from the classical theory of elasticity. To obtain the bond stretch and the bond shear deformation along a specific bond direction, the strain vector

$$\{\chi\} = \{s_1 \quad s_2 \quad \gamma\}^T \tag{33}$$

that defines a specific deformation state of $H_{\mathbf{X}}$, is transformed into a coordinate system whose first axis is aligned with the bond and the second axis is orthogonal to the bond. In this way, being ψ the angle of inclination of a specific bond with respect to the horizontal direction we can write

$$s(\psi) = \frac{1}{2}[s_1 + s_2 + (s_1 - s_2)\cos 2\psi + 2\gamma \sin 2\psi] \tag{34}$$

$$\gamma(\psi) = \frac{1}{2}[(s_1 - s_2)\sin 2\psi - 2\gamma \cos 2\psi] \tag{35}$$

It is worth noting that when a PD unit cell (the neighborhood of $\mathbf{X}$ or the family of $\mathbf{X}$) is subjected to a specific deformation state defined by Eq.(33), s_1 and s_2 are equivalent to ϵ_1 and ϵ_2 of the

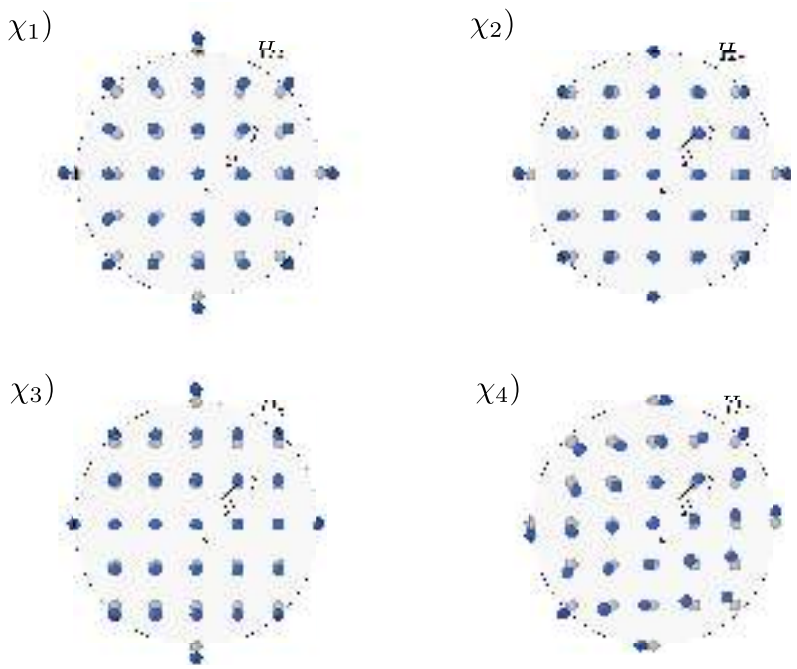

Figure 5: Schematics of region H_i subjected to: χ_1) isotropic expansion field of orthogonal PD stretch components s_1=s_2=s, $\gamma = 0$; χ_2) simple extension field of orthogonal PD stretch components s_1=s, $s_2 = \gamma = 0$; χ_3) simple extension field of orthogonal PD stretch components s_2=s, $s_1 = \gamma = 0$; χ_4) pure shear field of orthogonal PD stretch components s_1=s_2=0, $\gamma = s$.

continuum. However γ in our model is a single bond deformation measure, thus in a pure shear deformation state, γ=$\gamma^*/2$, where γ^* is the shear deformation of the continuum. The four deformation states considered are presented in Fig. 5, can be described by the following deformation tensors:

$$[\mathbf{F}]_1 = \begin{bmatrix} 1+s & 0 \\ 0 & 1+s \end{bmatrix}; \quad [\mathbf{F}]_2 = \begin{bmatrix} 1+s & 0 \\ 0 & 1 \end{bmatrix}; \quad [\mathbf{F}]_3 = \begin{bmatrix} 1 & 0 \\ 0 & 1+s \end{bmatrix}; \quad [\mathbf{F}]_4 = \begin{bmatrix} 1 & \gamma \\ \gamma & 1 \end{bmatrix} \tag{36}$$

which lead to the strain vectors

$$\{\chi\}_1 = \{s \quad s \quad 0\}^T \tag{37}$$

$$\{\chi\}_2 = \{s \quad 0 \quad 0\}^T \tag{38}$$

$$\{\chi\}_3 = \{0 \quad s \quad 0\}^T \tag{39}$$

$$\{\chi\}_4 = \{0 \quad 0 \quad 2\gamma\}^T \tag{40}$$

where $s << 1$ and $\gamma = s$. The conventional linear elastic strain energy density functions of the orthotropic continuum are obtained by

$$\phi(\mathbf{X})_1 = \frac{1}{2}C_{ij}\epsilon_i\epsilon_j = \frac{1}{2}\begin{bmatrix} C_{11} & C_{12} & 0 \\ C_{12} & C_{22} & 0 \\ 0 & 0 & C_{66} \end{bmatrix}\begin{Bmatrix} s \\ s \\ 0 \end{Bmatrix} \cdot \begin{Bmatrix} s \\ s \\ 0 \end{Bmatrix} = \frac{s^2}{2}(C_{11} + C_{22} + 2C_{12}) \tag{41}$$

$$\phi(\mathbf{X})_2 = \frac{1}{2}C_{ij}\epsilon_i\epsilon_j = \frac{1}{2}\begin{bmatrix} C_{11} & C_{12} & 0 \\ C_{12} & C_{22} & 0 \\ 0 & 0 & C_{66} \end{bmatrix}\begin{Bmatrix} s \\ 0 \\ 0 \end{Bmatrix} \cdot \begin{Bmatrix} s \\ 0 \\ 0 \end{Bmatrix} = \frac{s^2}{2}\, C_{11} \tag{42}$$

$$\phi(\mathbf{X})_3 = \frac{1}{2}C_{ij}\epsilon_i\epsilon_j = \frac{1}{2}\begin{bmatrix} C_{11} & C_{12} & 0 \\ C_{12} & C_{22} & 0 \\ 0 & 0 & C_{66} \end{bmatrix}\begin{Bmatrix} 0 \\ s \\ 0 \end{Bmatrix} \cdot \begin{Bmatrix} 0 \\ s \\ 0 \end{Bmatrix} = \frac{s^2}{2}\, C_{22} \tag{43}$$

$$\phi(\mathbf{X})_4 = \frac{1}{2}C_{ij}\epsilon_i\epsilon_j = \frac{1}{2}\begin{bmatrix} C_{11} & C_{12} & 0 \\ C_{12} & C_{22} & 0 \\ 0 & 0 & C_{66} \end{bmatrix}\begin{Bmatrix} 0 \\ 0 \\ 2\gamma \end{Bmatrix} \cdot \begin{Bmatrix} 0 \\ 0 \\ 2\gamma \end{Bmatrix} = 2\gamma^2\, C_{66} \tag{44}$$

The peridynamic microelastic energy functions corresponding to the four deformation states described by Eqs. (37)-(40) are obtained substituting Eqs. (31)-(32) and Eqs. (34)-(35) in Eq.(17)

$$\begin{aligned}\Phi(\mathbf{X})_1 &= \frac{1}{2}\int_{H_{\mathbf{X}}} \frac{k_n(\psi)s^2\,|\boldsymbol{\xi}|}{2}\mathrm{d}V_{\mathbf{X}'} \\ &= \frac{1}{2}\int_0^{\delta} 4\int_0^{\pi/2} \frac{k_n(\psi)ts^2\,|\boldsymbol{\xi}|^2}{2}\mathrm{d}\psi\mathrm{d}\xi \\ &= \frac{t\pi s^2\delta^3}{48}(3k_{n_1}+3k_{n_2}+4k_{t_1}+2k_v)\end{aligned} \tag{45}$$

$$\begin{aligned}\Phi(\mathbf{X})_2 &= \frac{1}{2}\int_{H_{\mathbf{X}}} \frac{k_n(\psi)s^2(1+\cos2\psi)^2\,|\boldsymbol{\xi}|}{8} + \frac{k_t(\psi)s^2(\sin2\psi)^2\,|\boldsymbol{\xi}|}{8}\mathrm{d}V_{\mathbf{X}'} \\ &= \frac{1}{2}\int_0^{\delta} 4\int_0^{\pi/2} \frac{k_n(\psi)ts^2(1+\cos2\psi)^2\,|\boldsymbol{\xi}|^2}{8} + \frac{k_t(\psi)ts^2(\sin2\psi)^2\,|\boldsymbol{\xi}|^2}{8}\mathrm{d}\psi\mathrm{d}\xi \\ &= \frac{t\pi s^2\delta^3}{768}(38k_{n_1}+6k_{n_2}+24k_{t_1}+4k_v)\end{aligned} \tag{46}$$

$$\begin{aligned}\Phi(\mathbf{X})_3 &= \frac{1}{2}\int_{H_{\mathbf{X}}} \frac{k_n(\psi)s^2(1-\cos2\psi)^2\,|\boldsymbol{\xi}|}{8} + \frac{k_t(\psi)s^2(\sin2\psi)^2\,|\boldsymbol{\xi}|}{8}dV_{\mathbf{X}'} \\ &= \frac{1}{2}\int_0^{\delta} 4\int_0^{\pi/2} \frac{k_n(\psi)ts^2(1-\cos2\psi)^2\,|\boldsymbol{\xi}|^2}{8} + \frac{k_t(\psi)ts^2(\sin2\psi)^2\,|\boldsymbol{\xi}|^2}{8}\mathrm{d}\psi\mathrm{d}\xi \\ &= \frac{t\pi s^2\delta^3}{768}(6k_{n_1}+38k_{n_2}+24k_{t_1}+4k_v)\end{aligned} \tag{47}$$

$$\begin{aligned}\Phi(\mathbf{X})_4 &= \frac{1}{2}\int_{H_{\mathbf{X}}} \frac{k_n(\psi)\gamma^2(\sin2\psi)^2\,|\boldsymbol{\xi}|}{2} + \frac{k_t(\psi)\gamma^2(\cos2\psi)^2\,|\boldsymbol{\xi}|}{2}dV_{\mathbf{X}'} \\ &= \frac{1}{2}\int_0^{\delta} 4\int_0^{\pi/2} \frac{k_n(\psi)t\gamma^2(\sin2\psi)^2\,|\boldsymbol{\xi}|^2}{2} + \frac{k_t(\psi)t\gamma^2(\cos2\psi)^2\,|\boldsymbol{\xi}|^2}{2}\mathrm{d}\psi\mathrm{d}\xi \\ &= \frac{t\pi\gamma^2\delta^3}{192}(6k_{n_1}+6k_{n_2}+24k_{t_1}+4k_v)\end{aligned} \tag{48}$$

The system of four equations $\phi(\mathbf{X})_i = \Phi(\mathbf{X})_i$, $i = 1...4$

$$\begin{cases} s^2(C_{11}+C_{22}+2C_{12}) = \frac{t\pi s^2\delta^3}{24}(3k_{n_1}+3k_{n_2}+4k_{t_1}+2k_v) \\ s^2\,C_{11} = \frac{t\pi s^2\delta^3}{384}(38k_{n_1}+6k_{n_2}+24k_{t_1}+4k_v) \\ s^2\,C_{22} = \frac{t\pi s^2\delta^3}{384}(6k_{n_1}+38k_{n_2}+24k_{t_1}+4k_v) \\ 2\gamma^2\,C_{66} = \frac{t\pi\gamma^2\delta^3}{192}(6k_{n_1}+6k_{n_2}+24k_{t_1}+4k_v) \end{cases} \tag{49}$$

was solved, which resulted in:

$$k_{n_1} = \frac{12\,(C_{11} - C_{66})}{\pi t \delta^3} \tag{50}$$

$$k_{n_2} = \frac{12\,(C_{22} - C_{66})}{\pi t \delta^3} \tag{51}$$

$$k_{v} = \frac{12\,(3C_{12} - C_{66})}{\pi t \delta^3} \tag{52}$$

$$k_{t_1} = \frac{3\,(8C_{66} - C_{11} - C_{22} - 2C_{12})}{\pi t \delta^3} \tag{53}$$

which in the special case of isotropic material under plane stress conditions reduce to two independent constants

$$k_n = \frac{12\,(C_{11} - C_{66})}{\pi t \delta^3} = \frac{6E}{\pi t \delta^3 (1-\nu)} \tag{54}$$

$$k_t = \frac{3\,(8C_{66} - 2C_{11} - 2C_{12})}{\pi t \delta^3} = \frac{6E(1-3\nu)}{\pi t \delta^3 (1-\nu^2)} \tag{55}$$

whereas in plane strain conditions is

$$k_n = \frac{12\,(C_{11} - C_{66})}{\pi t \delta^3} = \frac{6E}{\pi t \delta^3 (1+\nu)(1-2\nu)} \tag{56}$$

$$k_t = \frac{3\,(8C_{66} - 2C_{11} - 2C_{12})}{\pi t \delta^3} = \frac{6E(1-4\nu)}{\pi t \delta^3 (1+\nu)(1-2\nu)} \tag{57}$$

Thus, by applying Eqs. (31) and (32), it is possible to assign a specific value to the axial and shear peridynamic springs constants, which are functions of the orientation ψ of the bond. In this way we can model the mechanical behavior of a full Cauchy orthotropic material. It is worth noting that the peridynamic model here introduced is a micropolar non-local lattice model. The particles rotational degree of freedom is necessary because of the fundamental requirement of rotational invariance. In fact the definition of a shearing deformation measure which does not account for particle rotations, could lead to an incorrect description of the mechanical behavior of materials undergoing non-homogeneous deformation fields. However, when referring to a Cauchy continuum, it should be reminded that the definition of an equivalent lattice model requires only 2 elastic moduli in isotropy (4 for in-plane orthotropy), and thus the definition of a rotational spring constant k_θ is somewhat redundant. A theoretical discussion of this aspect, that is related to the so called "Cauchy relations" which characterize the "rari-constant" material models, can be found in [47] while some examples of lattices were shown in [46]. The presence of further rotational moduli, which introduce internal

lengths into the parameters that govern the elasticity response, is otherwise needed when modelling an orthotropic micro-polar material, e.g. a Cosserat continuum, or when modelling at the macro-scale a composite material which has an internal periodic structure, which is explicitly affected by the size and shape of the internal microstructure [48]. In our case, it can improve the numerical performance of the discrete approximation in the case of non-homogeneous strain conditions, insofar as it allows to describe the case of variable axial bond forces with a reduced number of elements, since it can be seen as the addition of a linear term (in the bond force between two particles) in addition to the uniform axial bond force [48, 49]. In this sense, it can be stated that the introduction of the rotational stiffness term allows an improvement in the numerical behavior of the model implemented in situations of high strain gradient, especially in the case of a very coarse mesh. In this paper $k_\theta(\psi) = \frac{k_t(\psi)|\boldsymbol{\xi}|(1-|\boldsymbol{\xi}|/\delta)}{2}$ is used. The elastic shear parameter corresponding to Eqs.(55)-(57) are generalized stiffness which can satisfy the condition $k_t > 0$, $k_t < 0$, or $k_t = 0$. The case of $k_t = 0$, corresponding to $\nu = 1/3$ in plane stress and $\nu = 1/4$ in plane strain, is equivalent to consider a microelastic energy potential which depends only on the peridynamic bond stretch (being a bond shear deformation measure still definable in this condition). In the case of shear spring stiffness $k_t < 0$, the corresponding Poisson's ratio is larger than BBPD fixed values. A physical interpretation of negative shear spring stiffness, starting from molecular-dynamics consideration was given by [50]. The same considerations can be extended to the case of orthotropic materials. In any case, implicit solvers require that the global stiffness matrix is invertible, hence when dealing with negative bond stiffness, one has to be sure that this requirement is satisfied. Moreover it can be underlined that a micropolar peridynamic model with frame-like ligaments connecting particles, i.e. a 2D non-local lattice with Euler-Bernoulli beam-like microstructure (e.g. Gerstles model [38]), is a specific case of the model described in Sec. 2. In fact, as previously said, in Gerstle's micropolar peridynamic model each bond can be viewed as a micro cantilever Euler-Bernoulli beam with only two independent stiffness moduli, one related to stretch deformation and the other to bending effects (i.e. the ligament curvature). Another important consideration is that, contrary to the stiffness parameter d of Gerstle's micropolar model, the shear stiffness parameter k_t that characterize the micropolar

Table 1: Properties of the three orthotropic materials considered as example.

ID Material	E_1 (MPa)	E_2 (MPa)	ν_{12}	G (MPa)
1	15000	10000	0.3	8000
2	10000	10000	0.1	3000
3	200000	50000	0.25	50000

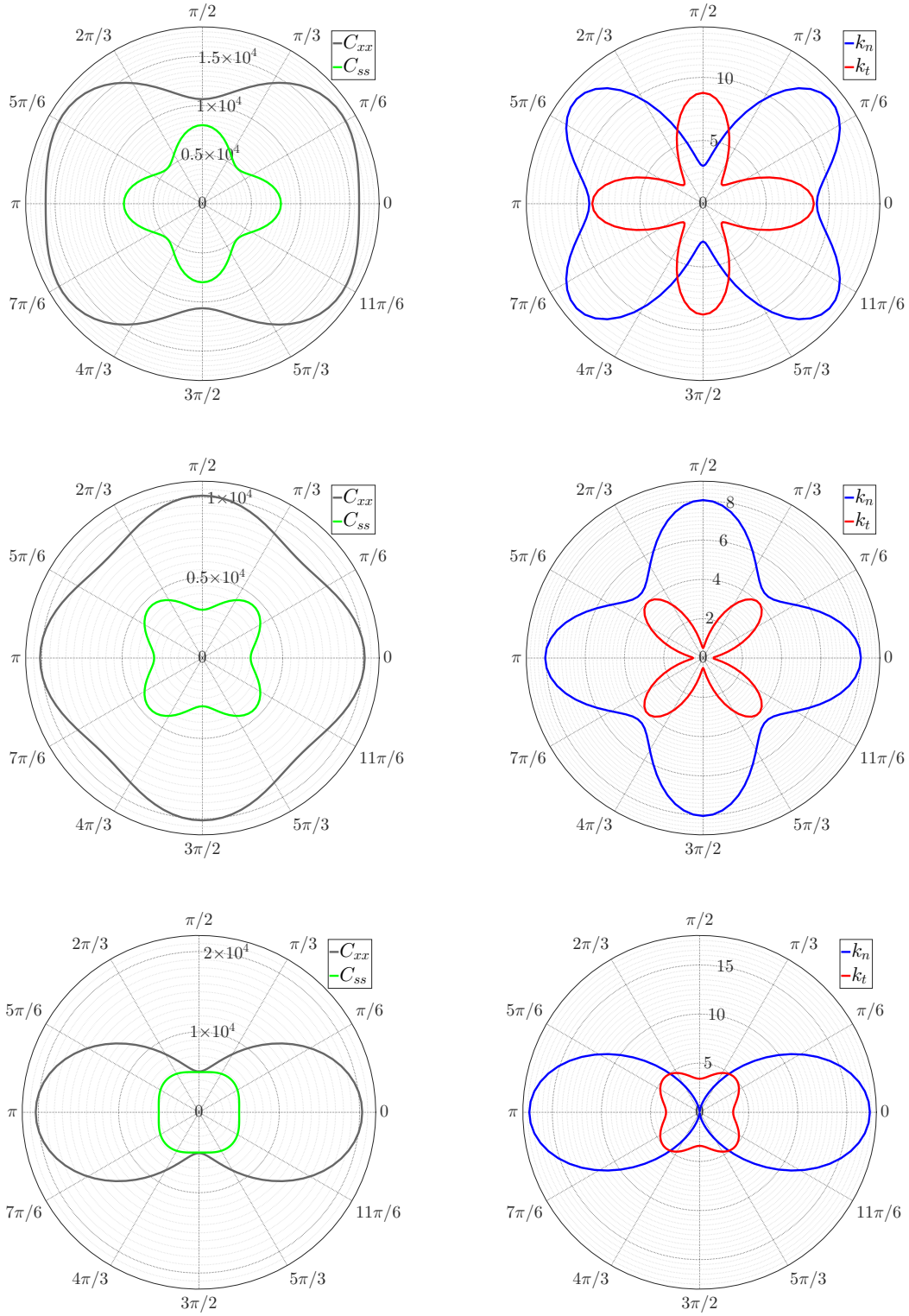

Figure 6: Comparison of the off-axis C_{xx} and C_{ss} classical continuum moduli (in MPa) and k_n and k_t MPPD moduli (in N/mm^6) for three examples of orthotropic material (First row: Material 1; Second row: material 2; Third row: material 3).

model proposed by the authors [36], has the same dimensions of the normal stiffness parameter k_n and is conceptually related to the shear modulus G of classical elasticity. This because the stiffness

k_t is directly related to the shear bond forces through a specific shear deformation parameter, similarly to the relationship among G, τ and γ^* in classical elasticity. To this end we show in Fig. 6 the comparison of the off-axis classical continuum moduli C_{xx} and C_{ss} classical continuum moduli peridynamic spring constants k_n and k_t, in the case of three different orthotropic materials whose properties are described in Tab. 1. As can be seen from Figs. 6, the polar plots of the normal and shear spring stiffnesses k_n and k_t, because of Eqs 31 and 32, have the same shape of that of C_{xx} and C_{ss} and they differs only of a scale factor.

3. Validation of the full orthotropic peridynamic model in elasticity

The capability of the PD micropolar formulation to describe a complex non-homogeneous elastic deformation field has been put to the test by modelling a rectangular lamina (a=400mm, b=200mm and unitary thickness) with a central hole of radius r=40mm subjected to simple extension (see Fig. 7). The discretized lattice model is composed by 2992 particles (a regular grid of 80×40 particles with $\delta = 0.2a$ is used) and the pre-existing center hole is introduced by removing the particles within the radius r and then by breaking all of the interactions passing through hole surfaces at the start of the simulation. The material properties of the specific orthotropic material are summarized in Tab. 2. Then, by applying Eqs. (31) and (32) together with Eqs. (50)-(53), the polar diagram of the axial and shear spring stiffnesses k_n and k_t are obtained (see Fig. 8). Five different orientations of the principal material directions, with respect to the horizontal direction, are considered (see Fig. 10). In this case, being $\zeta \neq 0$, Eqs.(31) and (32) can be rewritten in the general form

$$k_n(\psi-\zeta) = k_{n_1}\cos^4(\psi-\zeta)+k_{n_2}\sin^4(\psi-\zeta)+2k_\nu\sin^2(\psi-\zeta)\cos^2(\psi-\zeta)+4k_{t_1}\sin^2(\psi-\zeta)\cos^2(\psi-\zeta) \quad (58)$$

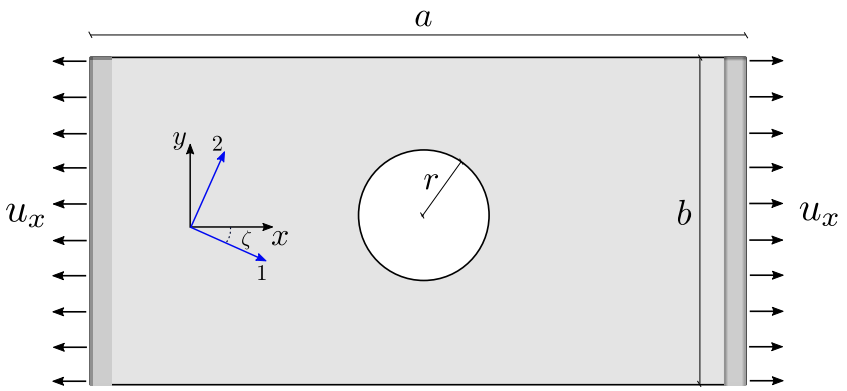

Figure 7: Schematics of boundary conditions of the rectangular lamina with hole subjected to an horizontal displacement field at boundaries.

$$k_t(\psi-\zeta) = k_{n_1}\sin^2(\psi-\zeta)\cos^2(\psi-\zeta) + k_{n_2}\sin^2(\psi-\zeta)\cos^2(\psi-\zeta) - 2k_v\sin^2(\psi-\zeta)\cos^2(\psi-\zeta) + k_{t_1}[\cos^2(\psi-\zeta) - \sin^2(\psi-\zeta)]^2 \tag{59}$$

Since we compare the peridynamic solution with the continuum elastic solution, a horizon/grid spacing ratio $m = \delta/\Delta x = 3.2$ has been considered, which gives a good compromise between accuracy of the (local) solution and the computational effort of the simulations [36]. The deformed shapes and displacement maps obtained with the PD model are compared to those obtained with Abaqus [51] FEM analyses [3]. The horizontal displacements are applied to the vertical boundary layers of thickness $\varrho = \delta$, resulting in the system configuration of Fig.7 (no constrains to the vertical displacements are imposed). As it can be seen, predicted patterns and values of displacement fields match well with FEM solutions (see Figs.11-15). A detailed quantitative comparison of two displacement components at the upper edge of the specimen is shown in Figs.16-17 that confirm

[3] In FEM analyses we considered an irregular mesh composed by 3548 four nodes squared plane-stress elements.

Table 2: Material properties

Property	Value
E_1	15000 MPa
E_2	5000 MPa
ν_{12}	0.25
G	4800 MPa
ρ	2500 kg/m^3

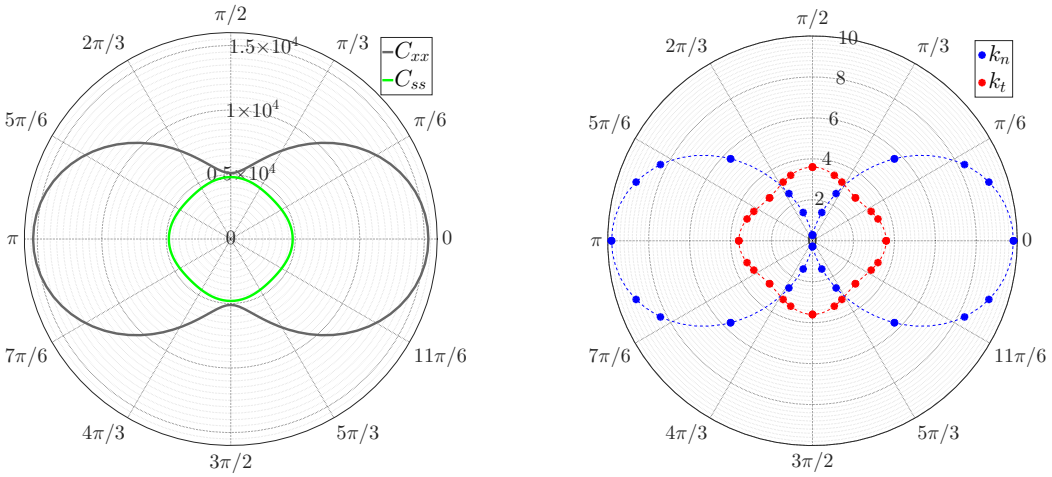

Figure 8: Comparison of the Off-axis C_{xx} and C_{ss} classical continuum moduli and k_n and k_t MPPD moduli (case of $\zeta = 0$).

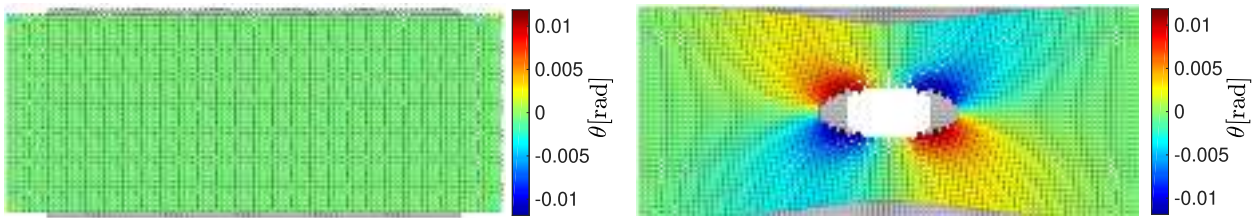

Figure 9: Maps of microrotations θ (visualized with OVITO software [52]) obtained with the proposed orthotropic peridynamic model and corresponding to the case of $\zeta = 0$: a) Simple lamina; b) Lamina with central hole.

the high accuracy of the proposed framework for modeling of orthotropic elasticity problems and thus the validity of the proposed orthotropic MPPD implementation.

It is worth noting that when the deformation field is homogeneous (as in the case of a simple lamina composed of isotropic material and subjected to simple extension) the rotational degree of freedom of the particles are not activated, thus a shearing deformation measure which does not take into ac-

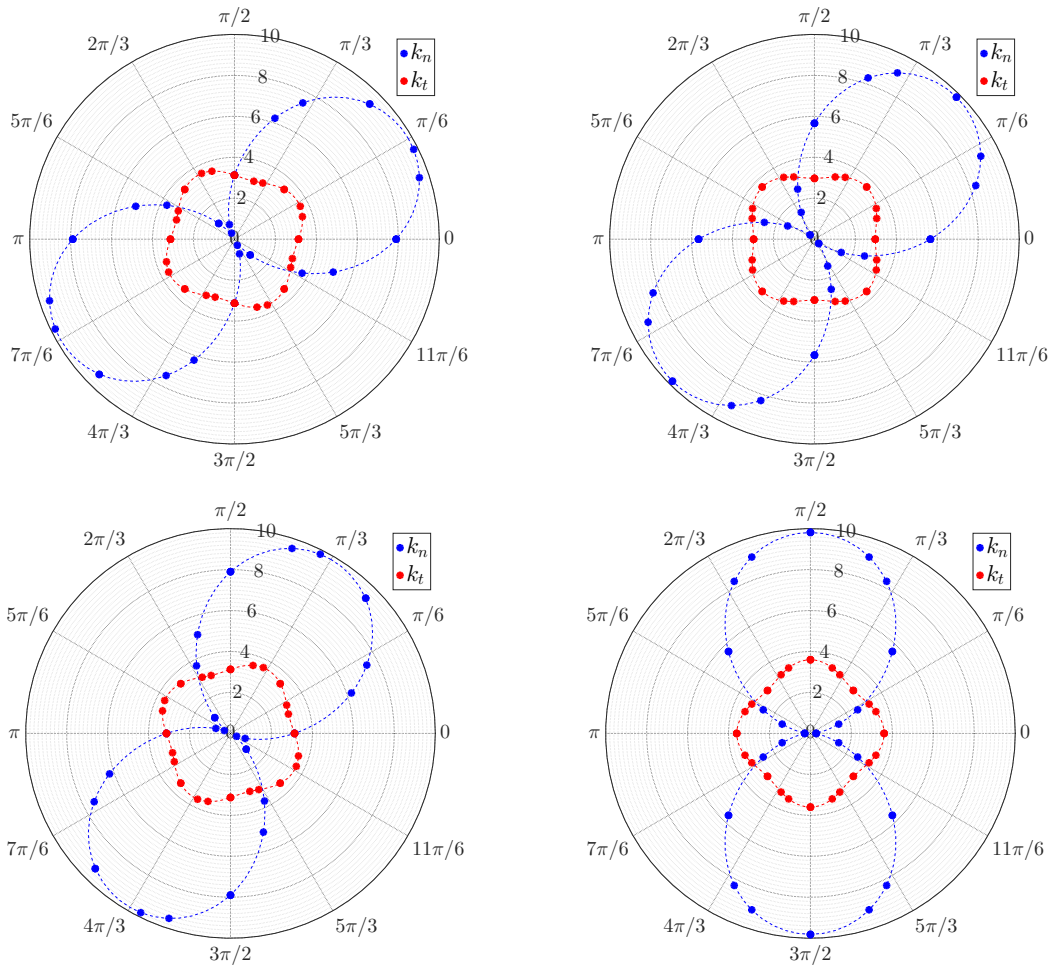

Figure 10: Off-axis k_n and k_t MPPD moduli in the case of $\zeta = \pi/6$, $\zeta = \pi/4$, $\zeta = \pi/3$ and $\zeta = \pi/2$.

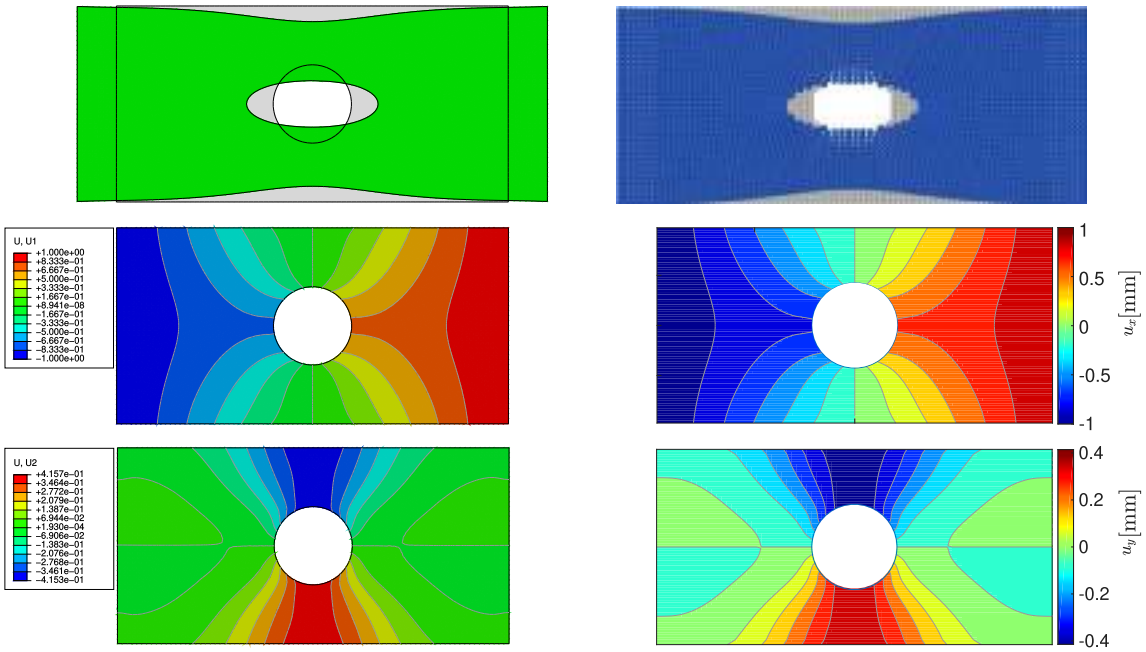

Figure 11: Simple traction, $\zeta = 0$: Deformed shape, horizontal and vertical displacements map obtained with FEM and orthotropic MPPD.

count particles rotations can be used. In other words a micropolar model is not strictly needed (see Fig. 9). However the deformation field of the lamina results in any case to be non-homogeneous, because of presence of the central hole, hence, when dealing with bond-based models with shear bond forces, a micropolar model is suggested for correctly describing the mechanical behavior of

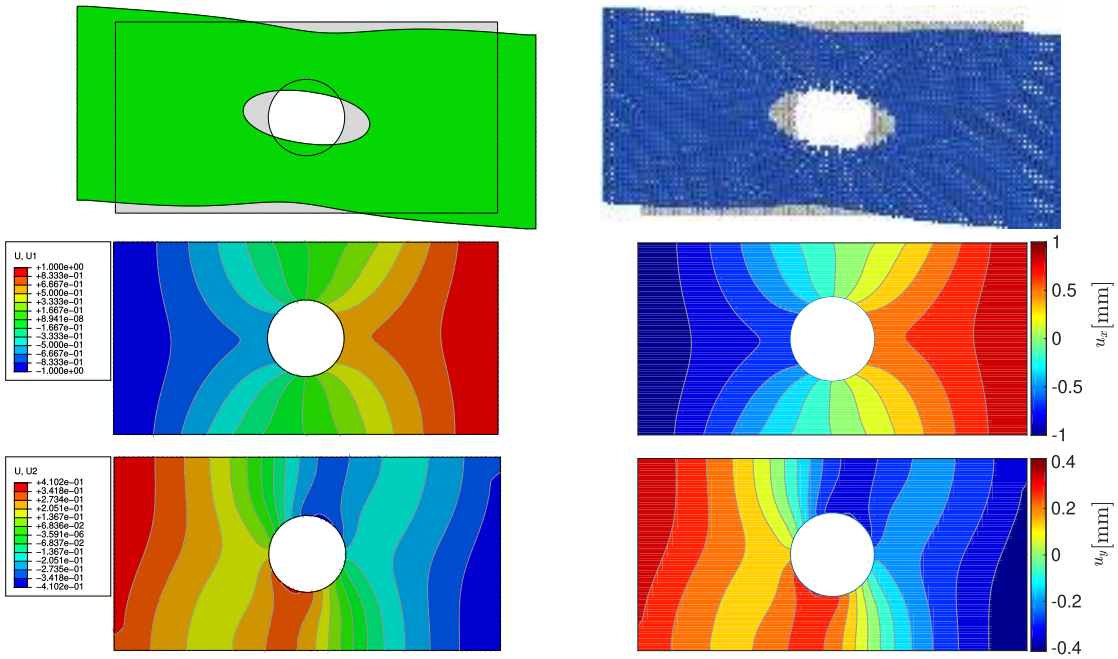

Figure 12: Simple traction, $\zeta = \pi/6$: Deformed shape, horizontal and vertical displacements map obtained with FEM and orthotropic MPPD.

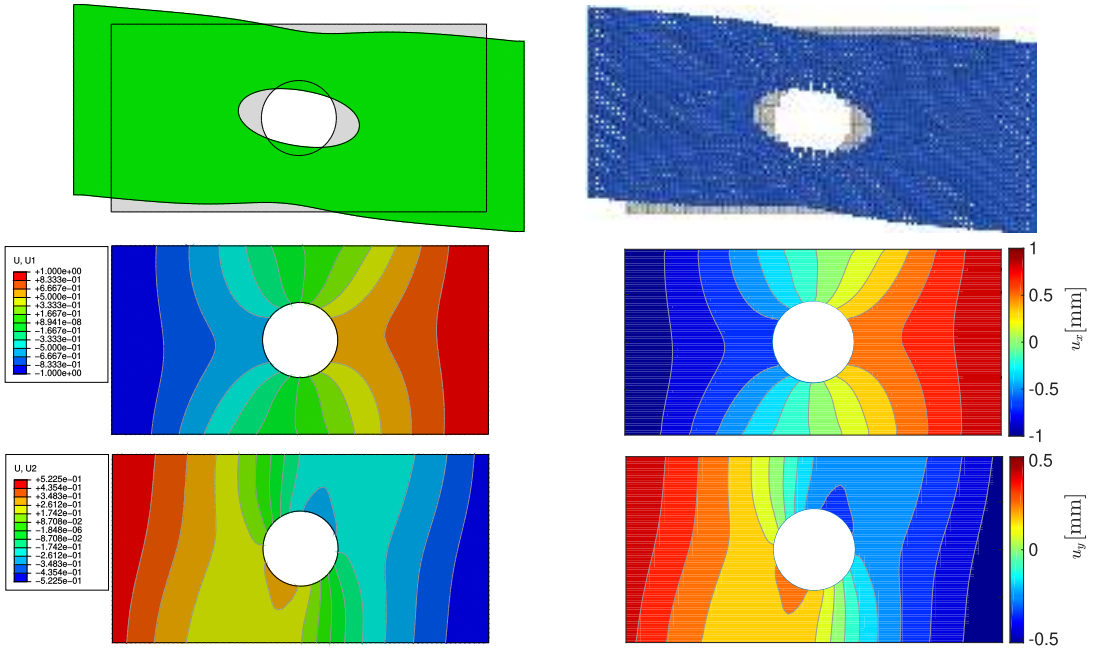

Figure 13: Simple traction, $\zeta = \pi/4$: Deformed shape, horizontal and vertical displacements map obtained with FEM and orthotropic MPPD.

the structure, since in lattice models the rotational degree of freedom is activated when a non-homogeneous deformation field involves local rotations [4]. Under these conditions, and when the

[4] A lamina made by orthotropic material and subjected to simple extension, experiences a deformation field which is in general non-homogeneous unless $\zeta = 0$ or $\zeta = \pi/2$.

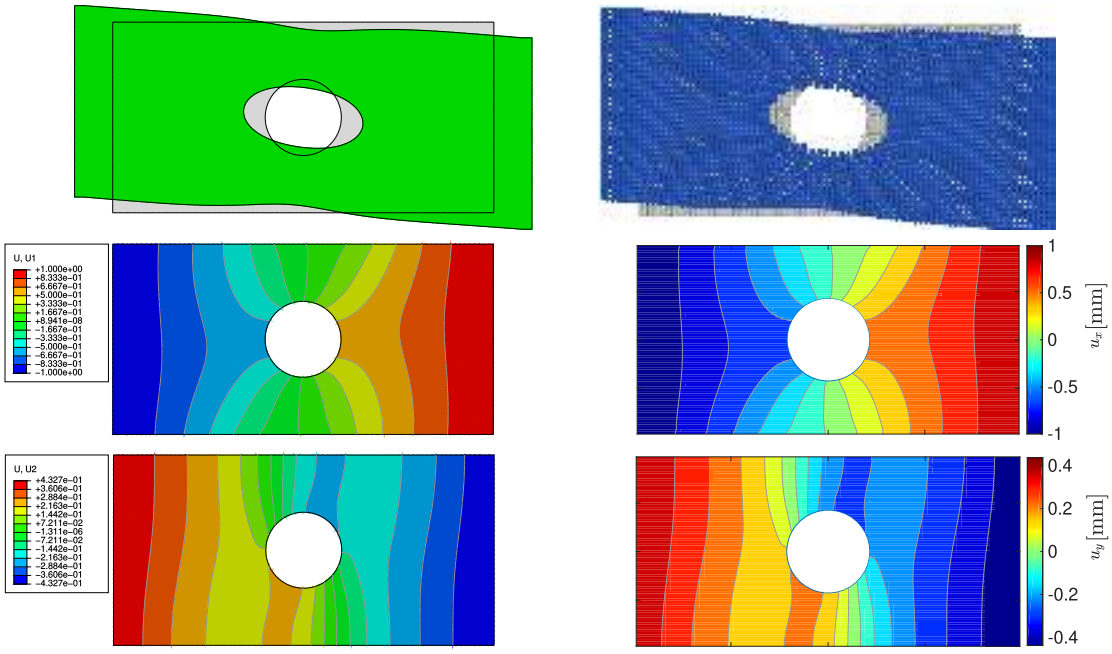

Figure 14: Simple traction, $\zeta = \pi/3$: Deformed shape, horizontal and vertical displacements map obtained with FEM and orthotropic MPPD.

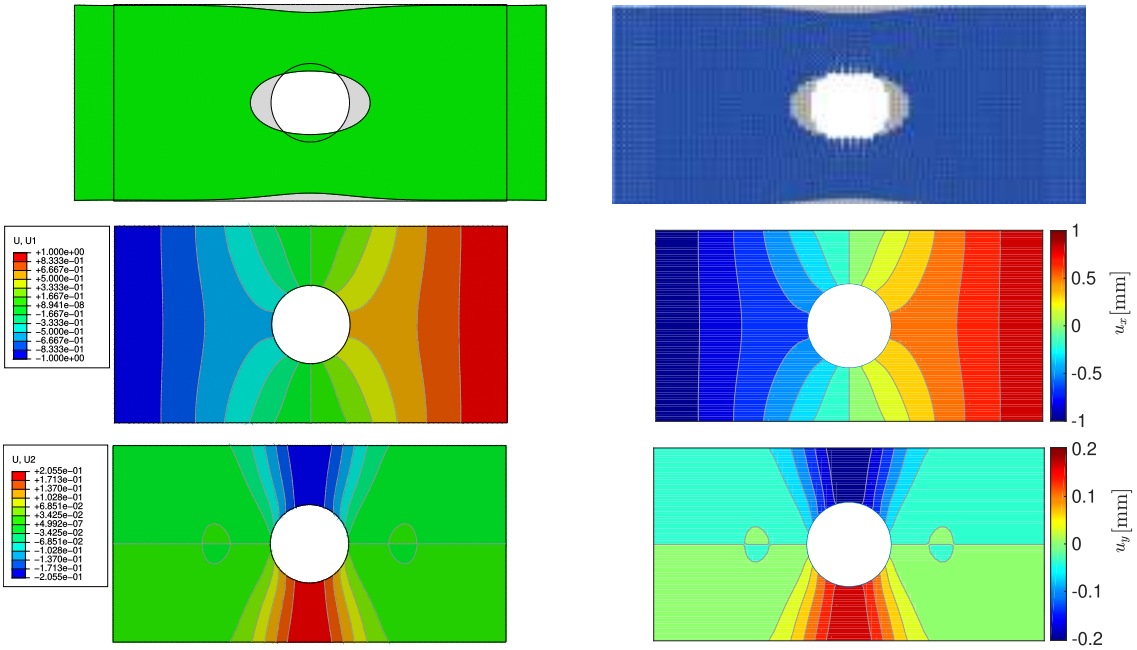

Figure 15: Simple traction, $\zeta = \pi/2$: Deformed shape, horizontal and vertical displacements map obtained with FEM and orthoropic MPPD.

shear bond stiffness of the lattice model is not null, the rotational invariance of the lattice unit cell may not be preserved in a non-micropolar bond-based model with single bond shear deformability [42]. The main reason, according to Jagota and Scherer [53], is that shear springs cannot distinguish the differences in the tangential displacement of two particles owing to a common rotation or shear. Thus, a global rigid body rotation may incorrectly result in an additional strain energy inside the shear springs [44, 42, 54]. As a result, the deformed configuration of the lamina predicted by a non-micropolar model, unless special treatment for solving this issue are used, [5] would appear to be not accurate, as shown in a previous work carried out by the authors [36].

3.1. Natural Frequency Analysis

A modal analysis is performed in order to evaluate the natural frequencies and the corresponding modal shapes of a square lamina with fixed base, by using the conceived orthotropic peridynamic model. The same rectangular lamina with a central hole is used in the simulations and the five different material frame orientation already described are considered. The generalized dynamic equilibrium of a BBPD model can be formulated by expressing the equilibrium of the effective

[5] Micropolar lattice models are physically-based models inspired by Voigt's studies on crystals [55], in which the microrotations and the micromoments ensure the balance of angular momentuum of the ligament. When using a non micropolar model which account for bond shear deformability, special treatment are needed for avoiding local rigid body rotations [42, 34, 56].

forces associated with each of its degrees of freedom. Then, neglecting the damping, the equilibrium equation is

$$[M]_{bond}\{\ddot{u}\} + [K]_{bond}\{u\} = \{p\} \tag{60}$$

where $[M]_{bond}$ is the bond mass matrix, $[K]_{bond}$ is the bond stiffness matrix and $\{p\}$ is the vector of external loads [57]. The model is meshfree and Lagrangian and the inertial properties of the lattice are concentrated in the particles centroyds, while zero mass is associated to the ligaments. Each particle i is given a mass $M_i = \Delta V_i \cdot \rho$ and a moment of inertia $J_i = M_i r_i^2$ (in the case of MPPD model), being r_i the radius of gyration associated to the particle, which in general is $r_i = 1/12(\Delta x^2 + \Delta y^2)$ [58]. The local mass matrix $[M]_{bond}$ may be highlighted by writing the kinetic

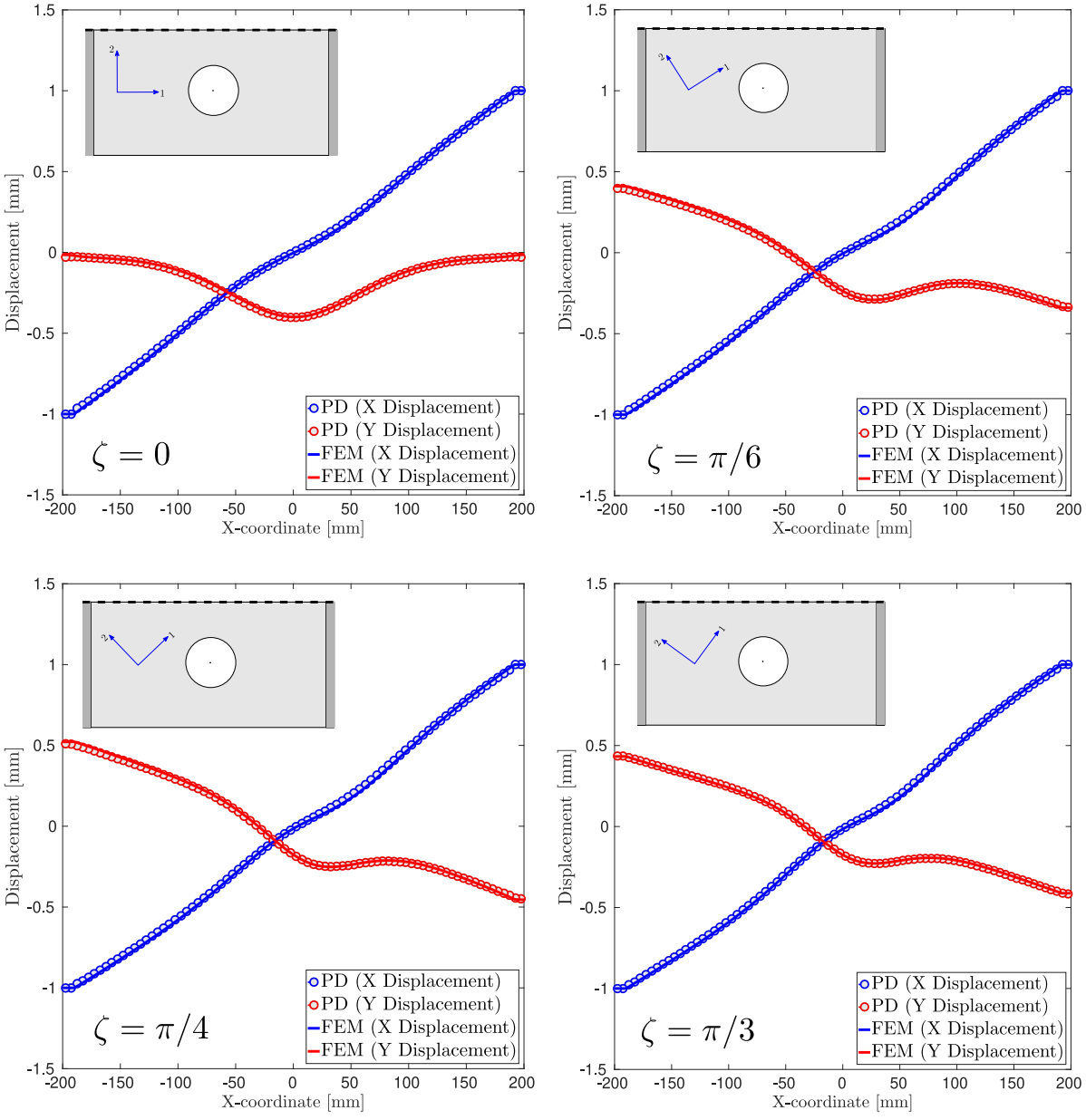

Figure 16: Displacements along the upper edge of the specimen in the case of $\zeta = 0$, $\zeta = \pi/6$, $\zeta = \pi/4$ and $\zeta = \pi/3$.

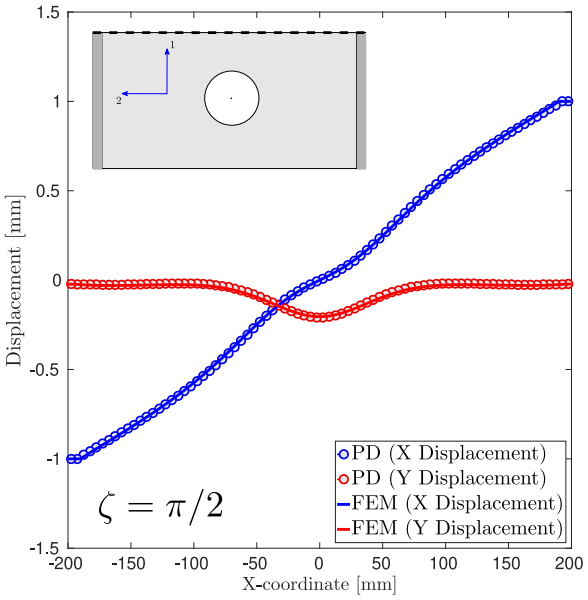

Figure 17: Displacements along the upper edge of the specimen in the case of $\zeta = \pi/2$.

energy of each particle in discrete form

$$\Pi(\dot{u}_x, \dot{u}_y, \dot{\theta}) = \frac{1}{2} M \dot{u}_x{}^2 + \frac{1}{2} M \dot{u}_y{}^2 + \frac{1}{2} J \dot{\theta}^2 \tag{61}$$

for MPPD model. The $[M]_{bond}$ matrix in the case of micropolar model is then

$$[M]_{bond} = \begin{bmatrix} \rho\Delta V_i & 0 & 0 & 0 & 0 & 0 \\ 0 & \rho\Delta V_i & 0 & 0 & 0 & 0 \\ 0 & 0 & \rho r_i^2 \Delta V_i & 0 & 0 & 0 \\ 0 & 0 & 0 & \rho\Delta V_j & 0 & 0 \\ 0 & 0 & 0 & 0 & \rho\Delta V_j & 0 \\ 0 & 0 & 0 & 0 & 0 & \rho r_j^2 \Delta V_j \end{bmatrix} \tag{62}$$

Omitting the applied external load vector $\{p\}$ in Eq. (60), and assuming that the free vibration motion of the bond is simple harmonic, an eigenvalue problem is obtained

$$[K]_{bond}\{u\} - \omega^2 [M]_{bond}\{u\} = \{0\} \tag{63}$$

where ω are the eigenvalues of the problems, related to the natural frequencies f by $\omega = 2\pi f$. Assembling the global matrices of the lamina, the first three modal shapes are obtained (see Tabs. 3-5 and Figs. 19-23). The natural shapes together with the corresponding natural frequencies of the lamina predicted by the orthotropic micropolar model are in perfect agreement with FEM solutions. Moreover the errors relative to the FEM solutions seems to be not particularly affected by the specific orientation of the material frame system, and even in the case of non grid-friendly

orientations of the material reference system (i.e. $\zeta = pi/6$, or $\zeta = pi/3$), they are less that 4%. A δ-convergence study [39] shows that the differences between the MPPD natural frequencies reported in Tabs.3-5 and those computed adopting a coarser mesh ($\delta = 0.4a$, 748 particles), are less that 1%. Whereas adopting a more refined mesh ($\delta = 0.1a$, 11988 particles) the maximum error with respect to FEM solution can be reduced to about 2% (see Fig.18).

Table 3: Natural frequency analysis: Synopsis of the of frequency values (Hz) and relative errors (%) corresponding to the I flexural natural modes calculated by FE and MPPD models.

ζ	f_I (FEM)	f_I (MPPD)	Er.$_{MPPD}$
0	400.85	412.82	2.89
$\pi/6$	365.65	377.08	3.12
$\pi/4$	330.69	340.45	2.86
$\pi/3$	296.61	301.25	1.54
$\pi/2$	263.76	256.30	2.92

Table 4: Natural frequency analysis: Synopsis of the of frequency values (Hz) and relative errors (%) corresponding to the I axial natural mode calculated by FE and MPPD models.

ζ	f_{II} (FEM)	f_{II} (MPPD)	Er.$_{MPPD}$
0	1403.00	1440.45	2.61
$\pi/6$	1261.22	1309.68	3.70
$\pi/4$	1099.10	1140.37	3.61
$\pi/3$	959.49	980.92	2.18
$\pi/2$	848.18	830.43	2.14

Table 5: Natural frequency analysis: Synopsis of the of frequency values (Hz) and relative errors (%) corresponding to the II flexural natural mode calculated by FE and MPPD models.

ζ	f_{III} (FEM)	f_{III} (MPPD)	Er.$_{MPPD}$
0	1625.10	1676.43	3.06
$\pi/6$	1490.44	1539.31	3.17
$\pi/4$	1390.65	1434.33	3.04
$\pi/3$	1292.50	1319.52	2.05
$\pi/2$	1191.32	1163.14	2.41

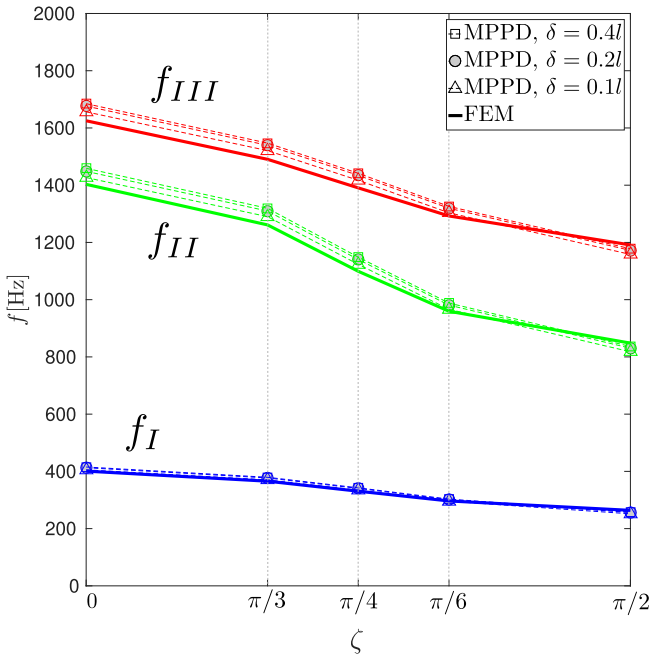

Figure 18: Natural frequency analysis: δ-convergence study carried out considering other two types of meshes and corresponding to ($\delta = 0.4a$, 748 particles) and ($\delta = 0.1a$, 11988 particles).

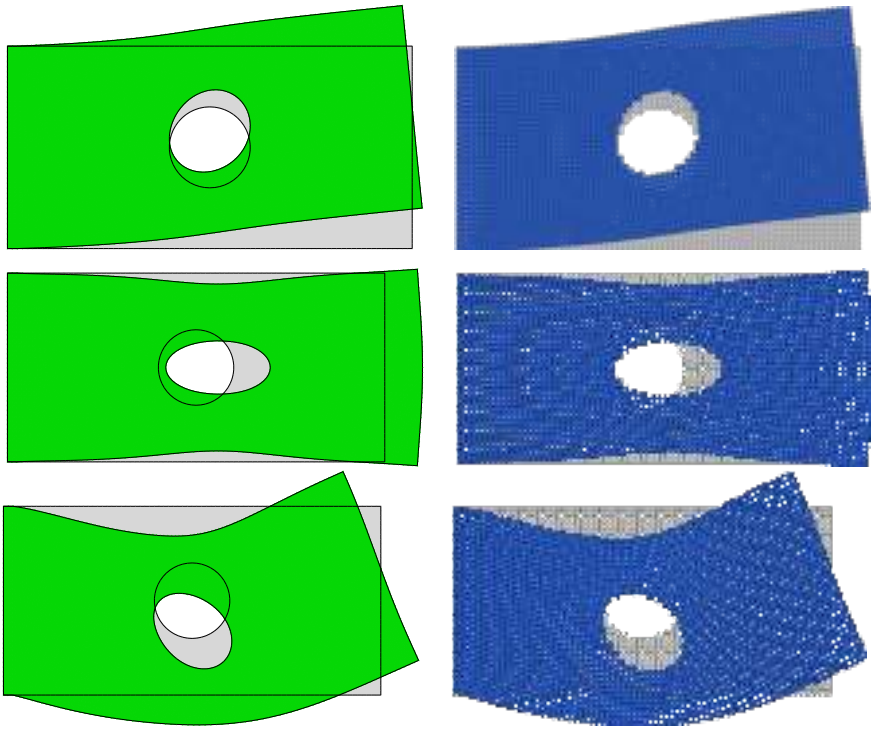

Figure 19: Natural Frequencies of the cantilever rectangular lamina, $\zeta = 0$: Deformed shapes obtained with FEM and proposed MPPD

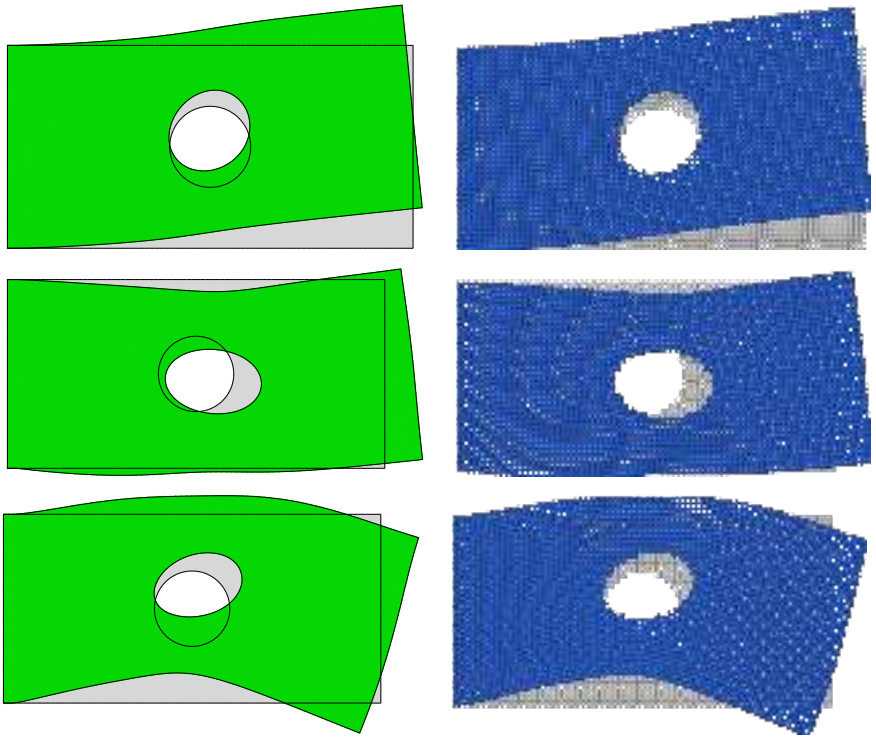

Figure 20: Natural Frequencies of the cantilever rectangular lamina, $\zeta = \pi/6$: Deformed shapes obtained with FEM and proposed MPPD.

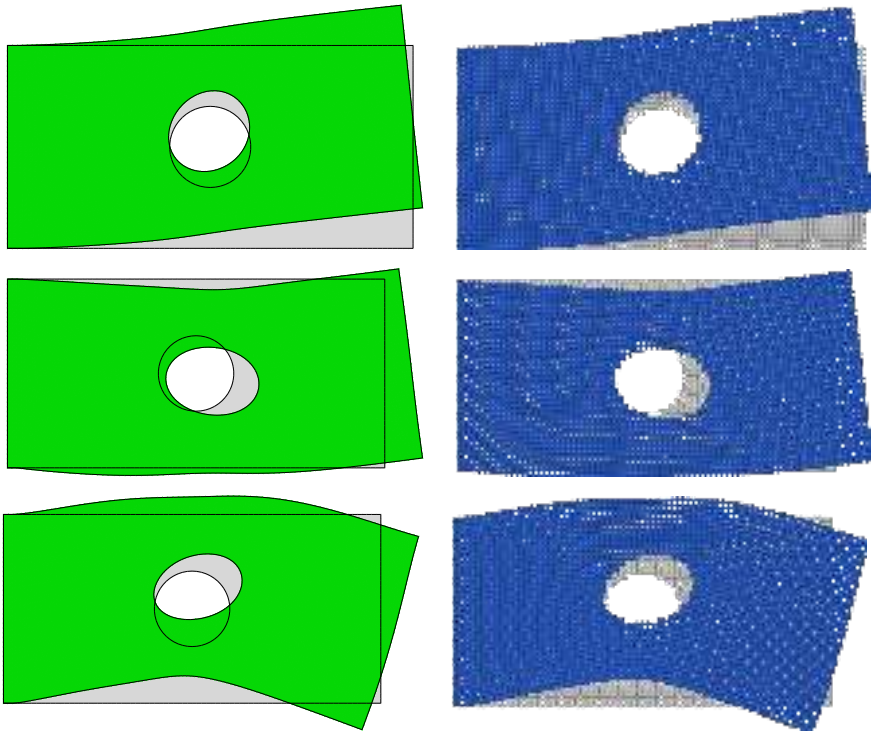

Figure 21: Natural Frequencies of the cantilever rectangular lamina, $\zeta = \pi/4$: Deformed shapes obtained with FEM and proposed MPPD.

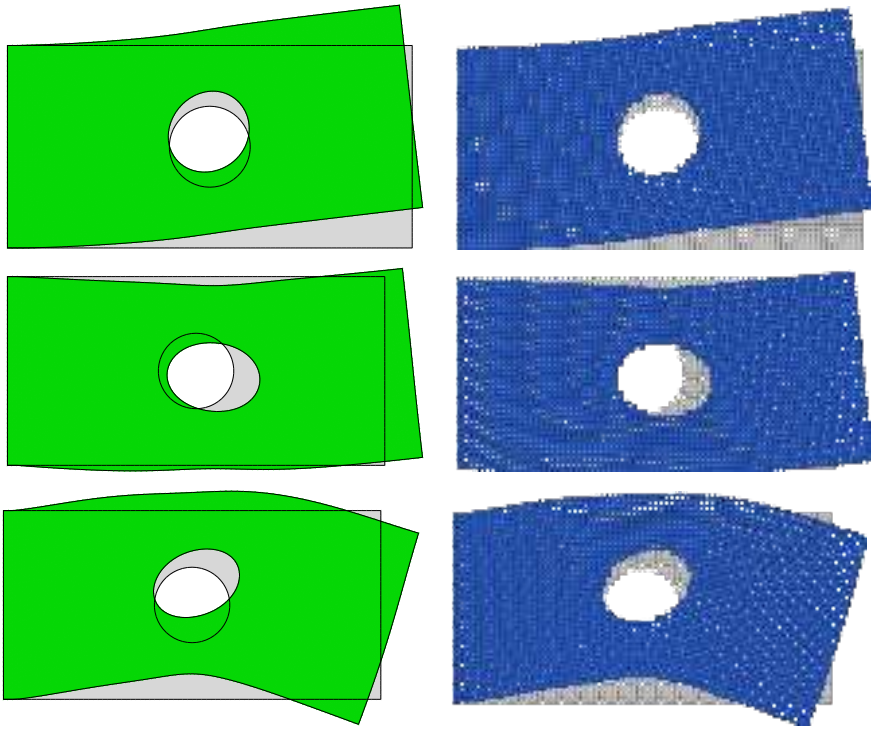

Figure 22: Natural Frequencies of the cantilever rectangular lamina, $\zeta = \pi/3$: Deformed shapes obtained with FEM and proposed MPPD.

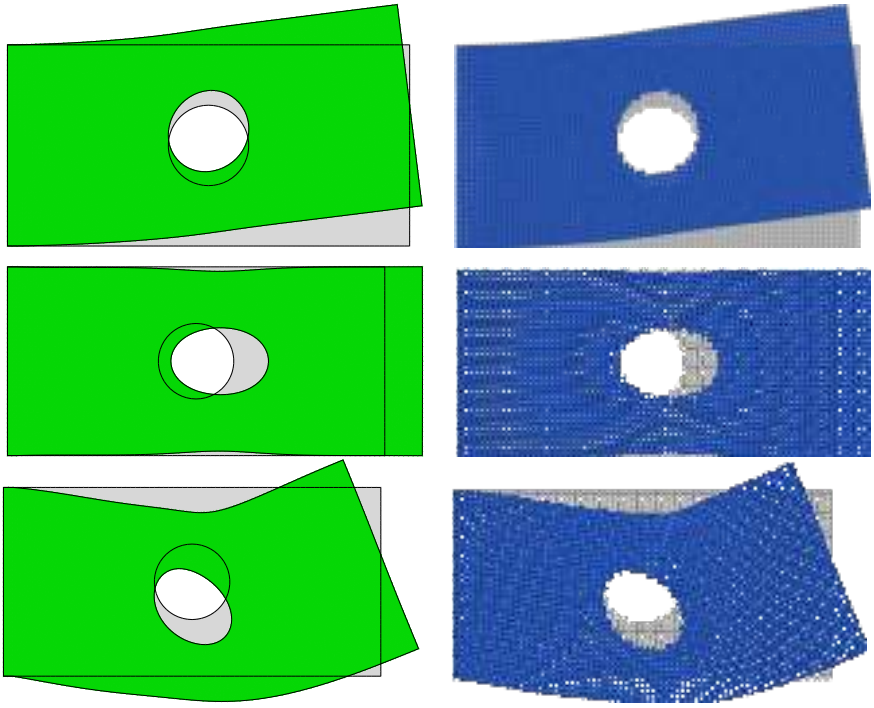

Figure 23: Natural Frequencies of the cantilever rectangular lamina, $\zeta = \pi/2$: Deformed shapes obtained with FEM and proposed MPPD.

4. Conclusions

In this paper a new 2D full orthotropic micropolar peridynamic model for linearly elastic solids has been proposed. For the first time a micropolar peridynamic formulation has been extended to non-isotropic materials and an orthotropic bond-based model characterized by four independent elastic moduli has been obtained. In fact, differently from other orthotropic bond-based models, the values of the Poisson's ratio ν_{12} and shear modulus G are not functions of the axial moduli. Another important feature of the model is that the bond properties, i.e. the stiffness constants, are continuous functions of the bond orientation in the principal material axes. The introduction of a bond shear stiffness, conceptually related to the shear modulus G of classical elasticity, and the definition of a specific bond shearing deformation measure which accounts for particle's rotations, lead to a physically-based model capable to predict the mechanical behavior of a wide variety of Cauchy orthotropic materials undergoing homogeneous and non-homogeneous deformations. The accuracy of the proposed model in linear elasticity has been verified through simulating uniaxial extension test of an orthotropic lamina with a central circular hole and natural frequency analysis considering five different orientations of the principal material reference system. Results obtained demonstrated the capabilities of the proposed framework for modeling of orthotropic elasticity problems. Future work is required to further extend the conceived model to general anisotropic materials and microstructural materials. Additional work is also planned to extend the proposed model to general 3D case, as well as the extension to anisotropic fracture.

References

[1] Silling, S.. Stability of peridynamic correspondence material models and their particle discretizations. Computer Methods in Applied Mechanics and Engineering 2017;322:42–57.

[2] Silling, S.. Reformulation of elasticity theory for discontinuities and long-range forces. Journal of the Mechanics and Physics of Solids 2000;48(1):175–209.

[3] Love, A.. A treatise on the Mathematical Theory of Elasticity. Dover, New York; 1944.

[4] Truesdell, C.. Timoshenko's History of Strength of Materials (1953). New York, NY: Springer New York; 1984, p. 251–253.

[5] Silling, S., Epton, M., Weckner, O., Xu, J., Askari, E.. Peridynamic states and constitutive modeling. Journal of Elasticity 2007;88(2):151–184.

[6] Warren, T.L., Silling, S.A., Askari, A., Weckner, O., Epton, M.A., Xu, J.. A non-ordinary state-based peridynamic method to model solid material deformation and fracture. International Journal of Solids and Structures 2009;46(5):1186 – 1195.

[7] Liu, W., Hong, J.W.. Discretized peridynamics for linear elastic solids. Computational Mechanics 2012;50(5):579–590.

[8] Wang, Y., Zhou, X., Wang, Y., Shou, Y.. A 3-d conjugated bond-pair-based peridynamic formulation for initiation and propagation of cracks in brittle solids. International Journal of Solids and Structures 2018;134:89 – 115.

[9] Wang, Y., Zhou, X., Shou, Y.. The modeling of crack propagation and coalescence in rocks under uniaxial compression using the novel conjugated bond-based peridynamics. International Journal of Mechanical Sciences 2017;128-129:614 – 643.

[10] Zhu, Q., Ni, T.. Peridynamic formulations enriched with bond rotation effects. International Journal of Engineering Science 2017;121:118 – 129.

[11] Gerstle, W., Sau, N., Silling, S.. Peridynamic modeling of concrete structures. Nuclear Engineering and Design 2007;237(12):1250 – 1258.

[12] Bobaru, F., Ha, Y., Hu, W.. Damage progression from impact in layered glass modeled with peridynamics. Central European Journal of Engineering 2012;2(4):551–561.

[13] Madenci, E., Oterkus, E.. Peridynamic theory and its applications. Springer New York; 2014.

[14] Casolo, S., Diana, V.. Modelling laminated glass beam failure via stochastic rigid body-spring model and bond-based peridynamics. Engineering Fracture Mechanics 2018;190:331 – 346.

[15] Shojaei, A., Mossaiby, F., Zaccariotto, M., Galvanetto, U.. An adaptive multi-grid peridynamic method for dynamic fracture analysis. International Journal of Mechanical Sciences 2018;144:600 – 617.

[16] Roy, P., Pathrikar, A., Deepu, S., Roy, D.. Peridynamics damage model through phase field theory. International Journal of Mechanical Sciences 2017;128-129:181 – 193.

[17] Madenci, E., Oterkus, S.. Ordinary state-based peridynamics for plastic deformation according to von mises yield criteria with isotropic hardening. Journal of the Mechanics and Physics of Solids 2016;86:192 – 219.

[18] Rahaman, M.M., Roy, P., Roy, D., Reddy, J.. A peridynamic model for plasticity: Micro-inertia based flow rule, entropy equivalence and localization residuals. Computer Methods in Applied Mechanics and Engineering 2017;327:369 – 391.

[19] Weckner, O., Mohamed, N.A.N.. Viscoelastic material models in peridynamics. Applied Mathematics and Computation 2013;219(11):6039 – 6043.

[20] Colavito, K., Kilic, B., Celik, E., Madenci, E., Askari, E., Silling, S.. Effects of nanoparticles on stiffness and impact strength of composites. Collection of Technical Papers - AIAA/ASME/ASCE/AHS/ASC Structures, Structural Dynamics and Materials Conference 2007;4:3950–3959.

[21] Xu, J., Askari, A., Weckner, O., Silling, S.. Peridynamic analysis of impact damage in composite laminates. Journal of Aerospace Engineering 2008;21(3):187–194.

[22] Hu, W., Ha, Y., Bobaru, F.. Modeling dynamic fracture and damage in a fiber-reinforced composite lamina with peridynamics. International Journal for Multiscale Computational Engineering 2011;9(6):707–726.

[23] Hu, Y., Madenci, E.. Bond-based peridynamic modeling of composite laminates with arbitrary fiber orientation and stacking sequence. Composite Structures 2016;153:139–175.

[24] Oterkus, E., Madenci, E.. Peridynamic analysis of fiber-reinforced composite materials. Journal of Mechanics of Materials and Structures 2012;7(1):45–84.

[25] Kilic, B., Agwai, A., Madenci, E.. Peridynamic theory for progressive damage prediction in center-cracked composite laminates. Composite Structures 2009;90(2):141 – 151.

[26] Hu, W., Ha, Y.D., Bobaru, F.. Peridynamic model for dynamic fracture in unidirectional fiber-reinforced composites. Computer Methods in Applied Mechanics and Engineering 2012;217-220:247 – 261.

[27] Askari, E., Bobaru, F., Lehoucq, R.B., Parks, M.L., Silling, S.A., Weckner, O.. Peridynamics for multiscale materials modeling. Journal of Physics: Conference Series 2008;125(1):012078.

[28] Ghajari, M., Iannucci, L., Curtis, P.. A peridynamic material model for the analysis of dynamic crack propagation in orthotropic media. Computer Methods in Applied Mechanics and Engineering 2014;276:431 – 452.

[29] Zhou, W., Liu, D., Liu, N.. Analyzing dynamic fracture process in fiber-reinforced composite materials with a peridynamic model. Engineering Fracture Mechanics 2017;178:60 – 76.

[30] Hu, Y., Yu, Y., Wang, H.. Peridynamic analytical method for progressive damage in notched composite laminates. Composite Structures 2014;108:801 – 810.

[31] Mikata, Y.. Linear peridynamics for isotropic and anisotropic materials. International Journal of Solids and Structures 2018;.

[32] Zhang, H., Qiao, P.. A state-based peridynamic model for quantitative elastic and fracture analysis of orthotropic materials. Engineering Fracture Mechanics 2019;206:147 – 171.

[33] Rabczuk, T., Ren, H.. A peridynamics formulation for quasi-static fracture and contact in rock. Engineering Geology 2017;225:42 – 48.

[34] Ren, H., Zhuang, X., Rabczuk, T.. A new peridynamic formulation with shear deformation for elastic solid. Journal of Micromechanics and Molecular Physics 2016;01(02):1650009.

[35] Zhang, G., Gazonas, G.A., Bobaru, F.. Supershear damage propagation and sub-rayleigh crack growth from edge-on impact: A peridynamic analysis. International Journal of Impact Engineering 2018;113:73 – 87.

[36] Diana, V., Casolo, S.. A bond-based micropolar peridynamic model with shear deformability: Elasticity, failure properties and initial yield domains. International Journal of Solids and Structures 2019;160:201 – 231.

[37] Matlab, . Matlab 2017a (programmimng language) 2017;.

[38] Gerstle, W., Sau, N., Sakhavand, N.. On peridynamic computational simulation of concrete structures. 265 SP; 2009, p. 245–264.

[39] Bobaru, F., Foster, J., Geubelle, P., Silling, S.. Handbook of peridynamic modeling. Advances in Applied Mathematics, CRC Press 2015;.

[40] Le, Q.V., Bobaru, F.. Surface corrections for peridynamic models in elasticity and fracture. Computational Mechanics 2017;.

[41] Karihaloo, B., Shao, P., Xiao, Q.. Lattice modelling of the failure of particle composites. Engineering Fracture Mechanics 2003;70(17):2385 – 2406.

[42] Pan, Z., Ma, R., Wang, D., Chen, A.. A review of lattice type model in fracture mechanics: theory, applications, and perspectives. Engineering Fracture Mechanics 2018;190:382 – 409.

[43] Lilliu, G., van Mier, J.. 3d lattice type fracture model for concrete. Engineering Fracture Mechanics 2003;70(7):927 – 941.

[44] Nikolić, M., Karavelić, E., Ibrahimbegovic, A., Miščević, P.. Lattice element models and their peculiarities. Archives of Computational Methods in Engineering 2017;.

[45] Gerstle, W.. Introduction to practical peridynamics: computational solid mechanics without stress and strain. World Scientific Publishing Co. Pte. Ltd.; 2016.

[46] Ostoja-Starzewski, M.. Lattice models in micromechanics. Applied Mechanics Reviews 2002;55(1):35–59.

[47] Stakgold, I.. The cauchy relations in a molecular theory of elasticity. Quarterly of Applied Mathematics 1950;8(2):169–186.

[48] Casolo, S.. Macroscopic modelling of structured materials: Relationship between orthotropic Cosserat continuum and rigid elements. International Journal of Solids and Structures 2006;43(3-4):475 – 496.

[49] Casolo, S.. Macroscale modelling of microstructure damage evolution by a rigid body and spring model. Journal of Mechanics of Materials and Structures 2009;4(3):551–570.

[50] Zhao, S.F., Zhao, G.F.. Implementation of a high order lattice spring model for elasticity. International Journal of Solids and Structures 2012;49(18):2568 – 2581.

[51] Smith, M.. ABAQUS/Standard User's Manual, Version 6.9. Simulia; 2009.

[52] Stukowski, A.. Visualization and analysis of atomistic simulation data with OVITO–the open visualization tool. Modelling and Simulation in Materials Science and Engineering 2009;18(1):015012.

[53] Jagota, A., Scherer, G.W.. Viscosities and sintering rates of a twodimensional granular composite. Journal of the American Ceramic Society 1993;76(12):3123–3135.

[54] Cusatis, G., Pelessone, D., Mencarelli, A.. Lattice discrete particle model (ldpm) for failure behavior of concrete. i: Theory. Cement and Concrete Composites 2011;33(9):881 – 890.

[55] Voigt, W.. Theoretische studien ber die elasticittsverhltnisse der krystalle. Abh Ges Wiss Gottingen 1887;34:3–51.

[56] Zhao, G.F., Fang, J., Zhao, J.. A 3d distinct lattice spring model for elasticity and dynamic failure 2011;35(8):859–885.

[57] Baraldi, D., Bullo, S., Cecchi, A.. Continuous and discrete strategies for the modal analysis of regular masonry. International Journal of Solids and Structures 2016;84:82 – 98.

[58] Bacigalupo, A., Gambarotta, L.. Wave propagation in non-centrosymmetric beam-lattices with lumped masses: Discrete and micropolar modeling. International Journal of Solids and Structures 2017;118-119:128 – 145.